Nano Research
2022, 15(4): 3675–3694

ISSN 1998-0124 CN 11-5974/O4
https://doi.org/10.1007/s12274-021-3979-6

Review Article

Two-dimensional noble transition-metal dichalcogenides for nanophotonics and optoelectronics: Status and prospects

Yingwei Wang[§] (✉), Li Zhou[§], Mianzeng Zhong, Yanping Liu, Si Xiao, and Jun He (✉)

Hunan Key Laboratory of Nanophotonics and Devices, School of Physics and Electronics, Central South University, Changsha 410083, China
[§] *Yingwei Wang and Li Zhou contributed equally to this work.*

Received: 20 July 2021 / **Revised:** 28 September 2021 / **Accepted:** 5 November 2021

ABSTRACT

An emerging subclass of transition-metal dichalcogenides (TMDs), noble-transition-metal dichalcogenides (NMDs), has led to an increase in nanoscientific research in two-dimensional (2D) materials. NMDs feature a unique structure and several useful properties. 2D NMDs are promising candidates for a broad range of applications in areas such as photodetectors, phototransistors, saturable absorbers, and meta optics. In this review, the state of the art of 2D NMDs research, their structures, properties, synthesis, and potential applications are discussed, and a perspective of expected future developments is provided.

KEYWORDS

two-dimensional (2D) materials, noble transition metal dichalcogenides (NMDs), transition metal dichalcogenides (TMDs), synthesis strategies, $PtSe_2$, $PdSe_2$

1 Introduction

Two-dimensional (2D) materials, that is, independent flake crystals with a plane size greater than 100 nm, while only a single or a few atomic layers in thickness [1, 2], have inspired a new wave of nanoscale research and exploration since the discovery of graphene and its special properties. Atomically thin 2D nanosheets, especially monolayers, exhibit unique condensed-matter phenomena and unusual properties that are yet to be revealed in their bulk state [3–7]. The rapid progress of graphene fabrication methods and the explosive growth of graphene applications inspired numerous investigations of other analog graphene 2D materials such as transition-metal dichalcogenides (TMDs) [8–10], group-VA semiconductors [11–13], 2D metal-organic frameworks (MOFs) [14–17], transition metal carbides, nitrides and carbonitrides (MXenes) [18–22]. Several approaches to synthesize 2D materials exist. These include mechanical exfoliation (ME) [23–25], liquid-phase exfoliation (LPE) [3, 26, 27], chemical vapor deposition (CVD) [28–33], hydrothermal/solvothermal methods [34–38]. In addition, 2D materials and their applications have a significant impact in a wide range of fields including optoelectronics [24, 39, 40], nanophotonics [41–43], energy storage [18, 44] and catalysis [45].

TMDs, in particular, may be of high interest for 2D-material-based applications [46, 47]. For example, TMDs exhibit a layer-dependent tunable bandgap that varies between 1 and 2 eV [3, 48]. This enables optical response in the near-infrared (NIR) and even middle infrared spectrum [49], which compensates for the zero band gap of graphene that is often undesirable. As an emerging subclass of TMDs, noble-transition-metal dichalcogenides (NMDs) with group 10 noble metals inspired nano-research of 2D materials. NMDs share the same formula, MX_2, where M denotes noble metals (Pt, Pd) and X refers to chalcogenides (S, Se, Te). Monolayer MX_2 NMDs generally contain two layers of X atoms and one layer of M atoms in a typical sandwich structure. Unlike most of the members of TMDs, the representative member of NMDs, $PtSe_2$, features a transition from metal to semimetal, when the layer number is reduced to a monolayer [50, 51]. Furthermore, a tunable bandgap in NMDs was confirmed by experimental and theoretical studies [52, 53]. Key properties of optoelectronic devices, i.e., high room temperature mobility, air-stable carrier mobility, were reported [54, 55]. In terms of nanophotonic applications, a broadband spectral response (extending even to the mid infrared [56]) was found, as well as a polarization-sensitive response to light [55, 57, 58]. Moreover, their defect-induced magnetism, with unique thickness-dependent properties, promises possible applications in spintronic devices [59, 60]. Considering these exceptional properties, NMDs have potential applications in a wide range of fields such as phototransistors [51, 61–63], gas sensors [64], saturable absorbers [65], photodetectors [58, 66, 67], electrocatalysis [68], flat optics [69], and anisotropic devices [70] (Fig. 1). However, to the best of our knowledge, a comprehensive review of structures, properties, syntheses, and potential applications of NMDs has not been published.

In this review, we summarize the latest progress of 2D NMDs concerning their structure, properties, synthesis, and potential applications. The review aims to provide insight into the opportunities and challenges associated with 2D-NMDs-based new physical phenomena and devices. We begin with a summary of the characteristics of NMDs, including structural configurations, electronic properties, optical properties, and magnetic properties. After an overview of the NMDs, we investigate several synthesis methods of NMDs that involve ME, LPE, and CVD. In addition, we highlight their potential

Address correspondence to Yingwei Wang, wyw1988@csu.edu.cn; Jun He, junhe@csu.edu.cn

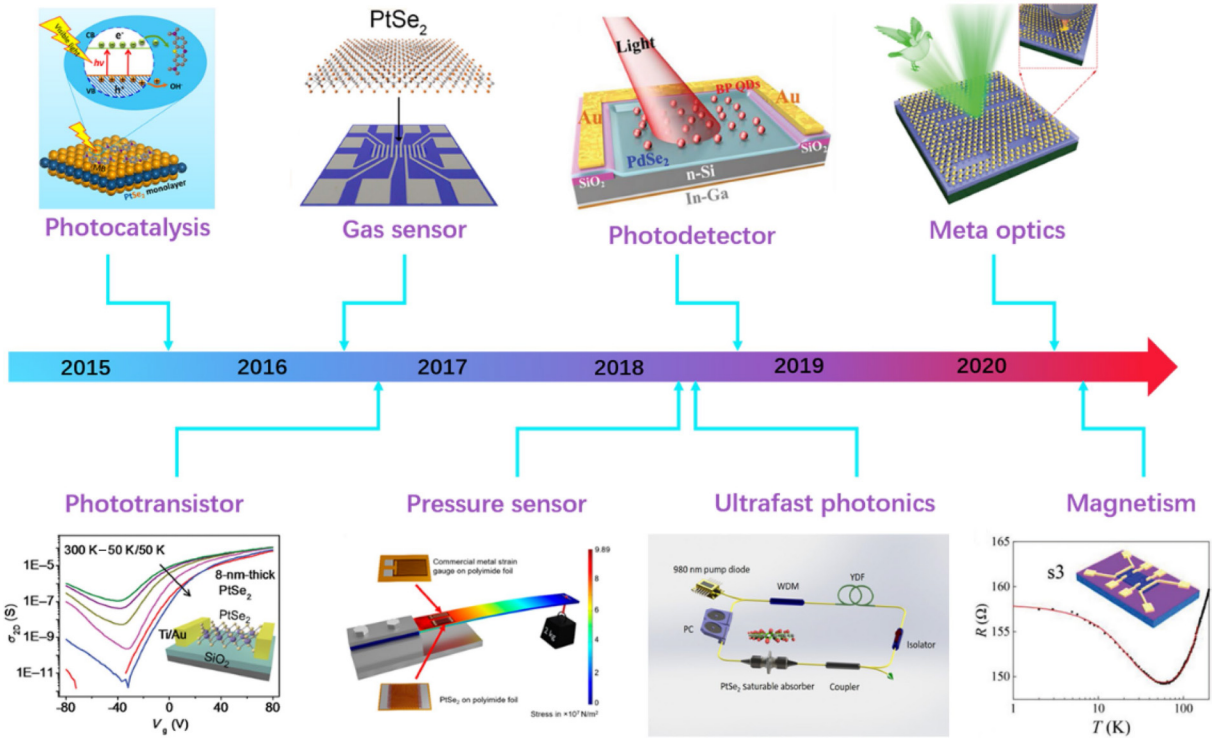

Figure 1 The development of the applications of NMDs (applications of NMDs in phototransistor, reproduced with permission from Ref. [62], © WILEY-VCH Verlag GmbH & Co. KGaA, Weinheim 2016; photodetector, reproduced with permission from Ref. [67], © WILEY-VCH Verlag GmbH & Co. KGaA, Weinheim 2018; meta optics, reproduced with permission from Ref. [69], © American Chemical Society 2020; photocatalysis, reproduced with permission from Ref. [50], © American Chemical Society 2015; gas sensor, reproduced with permission from Ref. [64], © American Chemical Society 2016; magnetism, reproduced with permission from Ref. [71], © Wiley-VCH GmbH 2020; pressure sensor, reproduced with permission from Ref. [72], © American Chemical Society 2018; ultrafast photonics, reproduced with permission from Ref. [73], © American Chemical Society 2018).

applications in areas like ultrafast photonics, field-effect transistors, photodetector, and meta optics. Finally, this review concludes with a brief overview of the latest research and anticipated research directions of 2D NMDs materials.

2 Fundamental properties of NMDs

2.1 Structure of NMDs

In recent years, TMDs have been investigated in depth. Most TMDs semiconductors possess a stable 2H phase [8, 62, 74]. In the 2H phase, the transition metals of the TMDs are located in the center of a triangular prism. From top to bottom, the metal atoms are surrounded by three chalcogen atoms [62]. The reported stable phases of monolayer TMDs are the 2H and 1T phases. Theoretically, 1T phase TMDs are the thermodynamic favorite, when the material is thinned down to a monolayer [53]. Similarly, the thermodynamically stable phase of NMDs is also a 1T phase. Thermodynamically stable 1T phases of $PdTe_2$ [75], $PtSe_2$ [56, 76], PtS_2 [61], $PtTe_2$ [77] were confirmed previously. These always show a typical octahedral structure [56], as shown in Figs. 2(a) and 2(b). They crystallize with a CdI_2-type structure, where each noble metal atom (Pd/Pt) within an octahedral hole is coordinated by six chalcogen atoms (S/Se/Te) to form an octahedron [8, 68]. A layer of Pt/Pd atoms is sandwiched between two layers of chalcogen atoms, and these layers are held together by van der Waal's forces. As the other two types of NMDs, $PdSe_2$ and PdS_2 exhibit the same stable phase structure, which differs from other NMDs. Unlike the previously mentioned NMDs with a symmetrical hexagonal structure, their atomic configuration shows a pentagonal arrangement in a plane (see Figs. 2(c) and 2(d)) [78]. Monolayer $PdSe_2$ consists entirely of pentagonal rings, where each Pd atom is combined with four Se/S atoms. This is different from the six coordinated transition metal atoms in the typical 1T and 2H structures of NMDs. Two adjacent Se/S atoms are connected by a Se–Se/S–S covalent bond [79, 80]. Due to the pentagonal structure of $PdSe_2$, the 2D $PdSe_2$ film also shows an asymmetric crystal structure, which is similar to black phosphorus (BP) and silicene [57].

2.2 Electronic properties

NMDs have attracted tremendous research interest into optoelectronic applications due to their unique electronic properties. The binding energy of the valence electron d-orbitals of group 10 transition-metals is very close to that of the valence electron p-orbitals of chalcogen atoms [68]. This enables a more extensive hybridization between group 10 metal d-orbitals and the chalcogen p-orbitals, compared to other TMDs. As a result, strong p and $d_{xz,yz}$ hybrid characteristics can be observed in NMDs, which suggests their distinct electronic properties [68].

The electronic band structure of NMDs was investigated using periodic density functional theory (DFT). Interestingly, when the MX_2 (M = Pt, Pd; X = S, Se, Te) monolayers behave like indirect bandgap semiconductors, the MSe_2 and MTe_2 analogues have significantly smaller bandgaps and can even become semi-metallic or metallic materials [53]. Hence it can be inferred that the electric properties of NMDs depend on the chalcogen atoms in the composition. For example, PtS_2 was found to be a semiconductor, whereas $PtTe_2$ was considered a metal [68]. In addition, the characteristics of the transition from semimetal to semiconductor are also related to the thickness of the NMDs (Fig. 3(a)) [67]. Bulk $PtSe_2$ is normally a semimetal with a zero bandgap. However, when the thickness approaches a monolayer, a semimetal-to-semiconductor transition occurs [64, 73].

Furthermore, the band structure of a material plays a critical role in optoelectronic and photonic applications. A customizable

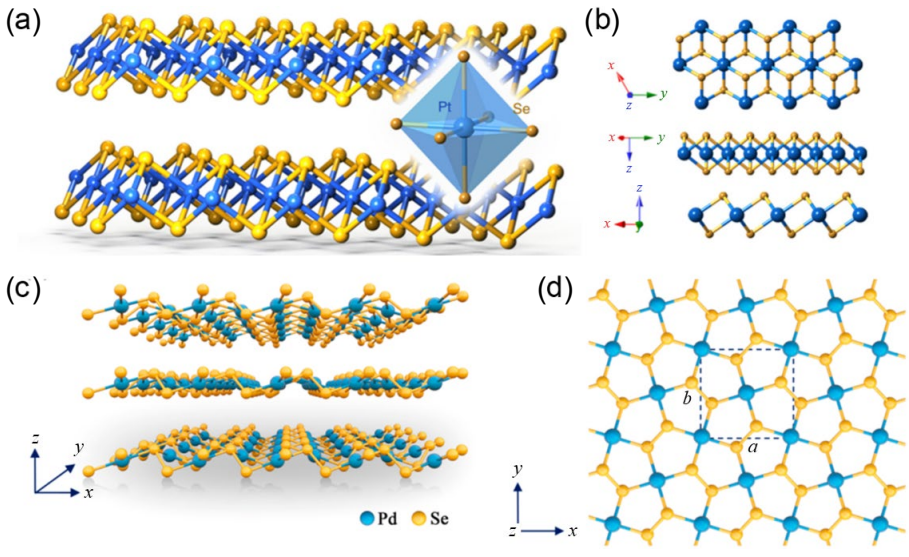

Figure 2 Crystal structure of NMDs. (a) and (b) A typical octahedral structure for $PdTe_2$, $PtSe_2$, PtS_2, and $PtTe_2$. Reproduced with permission from Ref. [56], © Yao, W. et al. 2017. (c) and (d) The puckered pentagonal crystal structure for PdS_2 and $PdSe_2$. Reproduced with permission from Ref. [78], © American Chemical Society 2020.

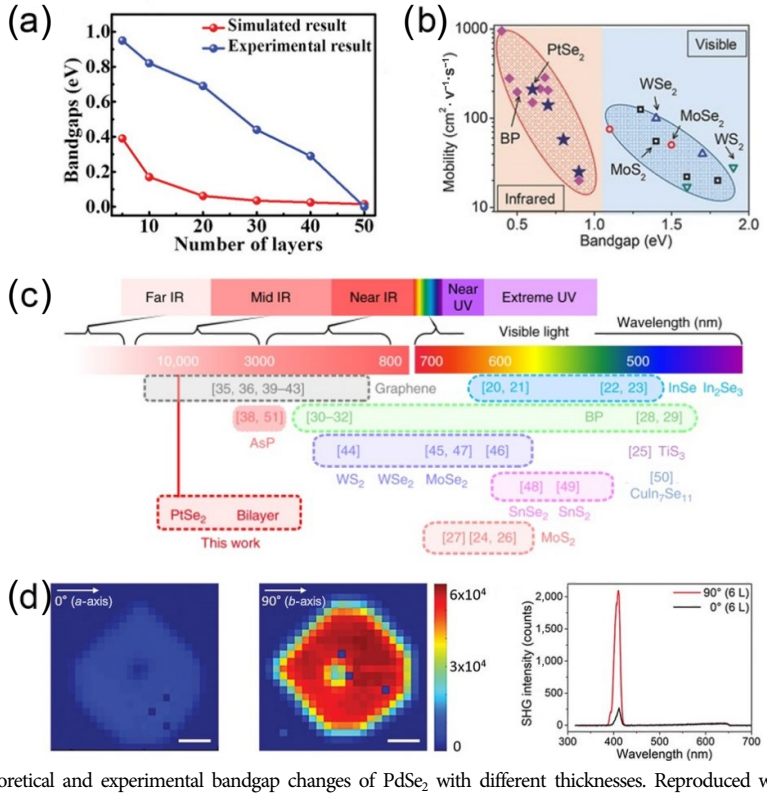

Figure 3 (a) Comparison of theoretical and experimental bandgap changes of $PdSe_2$ with different thicknesses. Reproduced with permission from Ref. [67], © WILEY-VCH Verlag GmbH & Co. KGaA, Weinheim 2018. (b) The layer-dependent mobility of $PtSe_2$, BP, and group-6 TMDCs at room temperature on back-gated SiO_2 substrate. Reproduced with permission from Ref. [62], © WILEY-VCH Verlag GmbH & Co. KGaA, Weinheim 2016. (c) Comparison of photodetectors operated at different wavelengths, based on two-dimensional materials. Reproduced with permission from Ref. [56], © Yu, X. C. et al. 2018. (d) Intensity maps of SHG emission from a $PdSe_2$ flake with 0° and 90° crystal orientations relative to the laser polarization. It is excited by an 800 nm laser and integrated between 380 and 450 nm. The scale bars are 1 μm. Reproduced with permission from Ref. [86], © WILEY-VCH Verlag GmbH & Co. KGaA, Weinheim 2020.

band structure is always a desirable and helpful feature of a candidate material for optoelectronics applications [67]. NMDs were found to feature a strong interlayer interaction and a widely tunable bandgap, which corresponded to a spectral range ranging from the visible to the infrared (Fig. 3(c)) [56, 61, 62]. For instance, $PdSe_2$ exhibits a widely tunable indirect bandgap (from 0 to 1.3 eV), when transitioning from bulk to monolayer, due to its strong interlayer-coupling [81]. This is different from other widely studied TMDs, which show an indirect-to-direct band structure transition for the transition from bilayer to monolayer [82]. A similar change, when transitioning from semiconductor (monolayer) to semimetal (bulk) of $PdSe_2$, was observed by other groups [67]. Moreover, PdS_2 and $PdTe_2$ also show a transition from semi-metallic in bulk structure to semiconductor properties in the monolayer [75, 80]. Pt dichalcogenides, which involve PtS_2, $PtSe_2$, and $PtTe_2$, show similar properties as Pd dichalcogenides. When the thickness approaches a single layer, $PtSe_2$ behaves like a semimetal to semiconductor transition. The indirect bandgaps of monolayer $PtSe_2$ and bilayer $PtSe_2$ are 1.2 and 0.2 eV, respectively [73]. In another report, the bandgap of bulk $PtSe_2$ was determined to be 0 eV, with semi-metallic properties and monolayer $PtSe_2$ being a semiconductor [50, 66, 72]. PtS_2 has a layer-dependent

indirect bandgap, ranging from 1.6 eV (monolayer) to 0.25 eV (bulk), which is even wider than that of BP [83]. Otherwise, for bulk PtX_2 (X = S, Se, Te) structures, PtS_2 is the only semiconductor among the three bulk structures [83]. Furthermore, $PtTe_2$ has the smallest monolayer bandgap (0.40 eV), which is also associated with semi-metallic properties, after transitioning from bilayer to bulk [84]. Interestingly, the polarity of NMDs also shows significant dependence on the number of layers. The electric transport measurements of a few-layered $PtSe_2$ indicate a unipolar p-type behavior. However, when the thickness is accurately measured to two layers, the polarity is changed to ambipolar [63].

Moreover, NMDs are predicted to have high carrier mobilities (more than 1,000 $cm^2 \cdot V^{-1} \cdot s^{-1}$) at room temperature [62, 85]. For example, Zhao et al. fabricated a few-layer $PtSe_2$ field-effect transistor, which showed high room-temperature mobility (≈ 210 $cm^2 \cdot V^{-1} \cdot s^{-1}$) in a back-gated configuration on SiO_2/Si. The mobility can be comparable to black phosphorus (Fig. 3(b)) [62]. Gu et al. showed that $PdSe_2$ had high carrier mobility and ambipolar properties. The group fabricated a field-effect transistor (FET) based on a few layers of $PdSe_2$. The FET revealed tunable bipolar charge carrier conduction with electron mobilities reaching 294 $cm^2 \cdot V^{-1} \cdot s^{-1}$ [86]. In addition, the high carrier mobility [87] and strong interlayer-coupling [81] of NMDs are also valuable properties.

2.3 Optical properties

Studying the optical properties of 2D materials is essential to determine whether a 2D material is suitable for optoelectronic devices. Due to the unique electronic properties and anisotropic atom structure of NMDs, they show many useful optical properties such as infrared (or even MIR) optical response and linear dichroism transitions [57, 78]. The optical properties of NMDs were investigated in previous theoretical and experimental studies, including linear and nonlinear optical properties.

NMDs also show strong absorption across a wide spectral range. The linear absorption of $PtSe_2$ was measured using an ultraviolet–visible–infrared (UV–vis–IR) absorption spectrometer. The results show that $PtSe_2$ exhibits strong absorption from 250 to 2,200 nm. In other words, it fully covers the visible to near-infrared wavelengths [73]. In addition, $PdSe_2$ has a narrow bandgap, which changes during the transition from a single layer (1.3 eV) to bulk (0 eV). Such a narrow bandgap could enable an optical response band ranging from deep ultraviolet (DUV) to mid-infrared (MIR) [57]. Additionally, NMDs are also promising anisotropic materials due to their low crystal symmetry. As a member of the NMD family, $PdSe_2$ with puckered pentagonal structure, exhibits potentially useful anisotropic optical response properties. $PdSe_2$ is proven to be polarization-sensitive according to polarization-dependent Raman spectroscopy and optical absorbance measurements with polarized light along a different axis [57]. Gu et al. used polarized Raman spectroscopy and second harmonic generation diagrams to reveal the in-plane optical anisotropy of $PdSe_2$ sheets (Fig. 3(d)) [86]. Another valuable property of NMDs is their capability to emit light. Recently, the photoluminescence (PL) of NMDs quantum dots (QDs) was determined. The optical properties of PdS_2 and $PdSe_2$ QDs exhibit excitation wavelength-dependent behavior. The reason for this may be related to the size of the QDs, i.e., the quantum size effect [88].

Because NMDs have strong optical absorption with a wide spectral range (DUV to MIR), they are ideal candidates for infrared photonics and optical communications. Their strong in-plane anisotropy makes them the best candidates for polarization-sensitive photodetectors. Furthermore, the PL properties of NMDs can be used for bioimaging and optical biosensing.

2.4 Magnetic properties

Magnetism plays an important role in both fundamental physics and many potential device applications. 2D magnetic materials are drawing worldwide attention due to their unique properties, including layer-dependent magnetism [89] and electric field modulation [90]. NMDs, type-II Dirac semimetals [91, 92], are interesting because of their layer-controllable metal-to-semiconductor transition [51, 93]. Several studies focused on the magnetic properties of NMDs in the last years.

The magneto-transport properties of ultrathin $PtSe_2$ crystals have also been investigated [60]. The electric measurements show that the number of layers in the sample determines the order of the ferromagnetic or antiferromagnetic ground states [60, 94]. The authors used first-principles calculations to show that surface magnetism, which was induced by the presence of Pt vacancies, and the Ruderman–Kittel–Kasuya–Yosida (RKKY) exchange coupling across ultrathin films of $PtSe_2$ were responsible for the observed layer-dependent magnetism. In addition, the defect-induced magnetism can be combined with the special thickness-dependent properties to realize spintronic devices with atomically thin materials [60]. Ge et al. reported a nearly thickness-dependent localized magnetic moment that was induced by Pt vacancies in air-stable type-II Dirac semimetal $PtSe_2$ flakes [71]. Their study offers a simple way to induce magnetism in non-magnetic materials. In addition, It is theoretically predicted that $PtSe_2$ has a superconducting transition at a very low temperature of 2 mK [95]. On the experimental side, the filamentous superconducting transition of wrinkled $PtSe_2$ at 2.3 K caused by rapid thermal treatment was observed [96]. The inhomogeneous strain induced by the thermal treatment caused the local superconducting islands to be formed in the wrinkled $PtSe_2$ with enhanced temperature.

Recently, the magnetoresistance (MR) in semiconducting trivial layered $PdSe_2$ flakes was investigated [97]. Due to the unique pentagonal crystal structure of $PdSe_2$, its anisotropic in-plane MR is unique. Specifically, when the magnetic field is perpendicular to the sample plane, the MR along the *a*-axis is significantly different from the MR along the *b*-axis.

In summary, so far there are relatively few reports on the application of NMDs in magnetism. Methods such as changing the number of layers of NMDs, defect induction, metal vacancies, and heat treatment can promote the magnetic applications of NMDs.

3 Preparation methods of NMDs

Recently, NMDs have attracted global attention across a wide range of fields. As discussed above, NMDs have many useful intrinsic properties, which can be used in electronics, optics and magnetic devices. To study their special properties in more detail and explore high-performance devices, it is necessary to synthesize high-quality bulk and 2D NMDs. In this section, we summarize the methods for the synthesis of NMDs, especially typical synthetic methods of 2D crystals. The chemical vapor transport (CVT) method as well as the self-flux method is the most common way to fabricate high-quality single-crystal NMDs. For the synthesis of 2D NMDs, the present approaches can be categorized as top-down strategy (ME, LPE, etc.) and bottom-up strategy (one-step CVD, two-step CVD, and MBE).

3.1 Preparation of bulk single crystal

There have been several reports on the preparation of bulk single crystal NMDs. The methods to synthesize single-crystal NMDs are mainly CVT and self-flux method. In addition, NMDs single crystals also exhibit metallic luster [61]. Yu et al. synthesized a $PtSe_2$ single crystal using the CVT method and compared it with

the CVD method. A schematic diagram of $PtSe_2$ single crystal growth is shown in Fig. 4(a). The size of $PtSe_2$ single crystals can reach 2–3 mm (Fig. 4(b)). Their surfaces are flat and without wrinkles, which indicates that the single-crystal samples, grown using this method, are of high quality [56].

A similar high-quality $PtSe_2$ crystal synthesis route was confirmed by another group, as shown in Fig. 4(c). In addition, the unique metallic properties and high electric conductivity were confirmed by constructing $PtSe_2$-based devices such as FETs [62]. This facile and convenient CVT method is very versatile for the synthesis of bulk NMDs. Li et al. used phosphorus as transport gas to synthesize PtS_2 single crystals via CVT. After the growth cycle, a plate-like crystal with a metallic luster and size of 6 mm × 6 mm × 0.2 mm was obtained [61]. The frequently used parameters in the NMDs synthesis based on CVT are summarized in Table 1. Recently, it has been reported that another method can be used to prepare NMDs single crystals, i.e., the self-flux method [54, 58, 98]. For example, Chow et al. reported $PdSe_2$ single crystals which were grown using a self-flux method [55]. The elements Pd and Se, using an atomic ratio of Pd:Se = 1:6, were mixed together and sealed in an evacuated quartz ampule. Then it was slowly heated to 850 °C and annealed for 50 h, Next, it was slowly cooled to 450 °C at a rate of 3 °C·h^{-1} down to room temperature. As a result, shiny single-crystal flakes can be obtained (Fig. 4(d)). Long et al. also synthesized $PdSe_2$ single crystals using the self-flux method. They used Pd powder mixed with Se powder (with an atomic ratio of 1:2) to prepare $PdSe_2$ polycrystalline powder in a tube furnace. Then, the prepared $PdSe_2$ polycrystalline powder and Se powder were mixed again with a mass ratio of 1:4 and placed in a tube furnace for heating. Finally, high-quality narrow-bandgap air-stable $PdSe_2$ single crystals were obtained (Fig. 4(e)) [58]. Single crystals of $PtTe_2$ can also be fabricated using the self-flux method. The authors directly mixed Pt foil and Te ingots, using a ratio of 1:17. To improve the quality of the crystals and remove the excess Te flux, the crystal was sealed again in a vacuum quartz tube and stored for four days at a constant temperature of 723 K. As a result, a crystal with a size of 8 mm × 8 mm × 1 mm was obtained [99]. Using a similar technique, Xu et al. also synthesized $PtTe_2$ crystals [98]. The transmission electron microscopy (TEM) image showed a lattice spacing of two groups of crystal plans. The lattice spacings were 0.211 and 0.117 nm which corresponded to the (110) and (100) planes of a hexagonal structure, respectively (Fig. 4(f)).

3.2 Preparation of 2D NMDs materials

As mentioned above, 2D NMDs always have unique and useful properties compared to the bulk material. Several ways to fabricate 2D NMDs were used (ME, LPE and CVD). The methods can be categorized into top-down methods and bottom-up methods.

3.2.1 Top-down methods

(a) ME

As shown in Figs. 5(a) and 5(b), the most common top-down methods are ME and LPE. ME is a common method to obtain 2D materials from bulk materials. In the case of NMDs, the researchers exfoliated few-layer (and monolayer) NMDs nanosheets from the synthesized high quality and single-crystalline bulk material. Li et al. used scotch tape-based ME method to mechanically peel off several layers of PtS_2 flakes from the corresponding bulk crystals. They transferred them to a Si substrate with 300 nm SiO_2 [61]. The thickness of the stripped PtS_2 atomic layer could reach about 2 nm. The exfoliated 2D PtS_2 retained the high-quality hexagonal single crystallinity of the CVT synthesized bulk PtS_2. Similarly, the octahedral structure $PtSe_2$ in the 1T phase (single crystal) can be peeled from bulk $PtSe_2$. The lateral dimension of monolayer $PtSe_2$ could reach several microns [62]. The high crystallinity of $PtSe_2$ enabled exceptional device performance and high room-temperature mobility (≈ 210 cm^2·V^{-1}·s^{-1}). Ciarrocchi et al. used ME method to obtain ultrathin $PtSe_2$ crystals. They also showed that $PtSe_2$ showed a bigger tuning range, with a complete transition from metal to a semiconductor, as the thickness was reduced [100].

The results of other groups confirmed the feasibility of the ME method to fabricate 2D NMDs [58, 83, 98]. ME method can yield the highest-quality monolayer or few-layer samples, which are ideal for the preparation of high-performance devices [8, 24]. But the ME method is not scalable and suitable for industrial production due to its high labor intensity, time-consuming, low

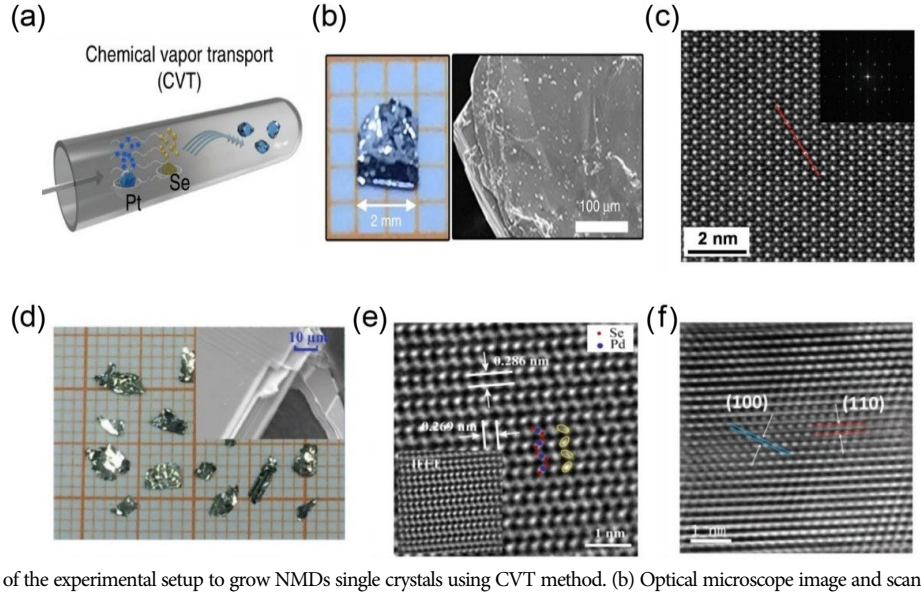

Figure 4 (a) Schematic of the experimental setup to grow NMDs single crystals using CVT method. (b) Optical microscope image and scanning electron microscope (SEM) image of the synthesized $PtSe_2$ flakes. Reproduced with permission from Ref. [56], © Yu, X. C. et al. 2018. (c) Experimental morphology STEM images of $PtSe_2$. Reproduced with permission from Ref. [62], © WILEY-VCH Verlag GmbH & Co. KGaA, Weinheim 2016. (d) Photographs of the as-grown $PdSe_2$ single crystals. Reproduced with permission from Ref. [55], © WILEY-VCH Verlag GmbH & Co. KGaA, Weinheim 2017. (e) Experimental morphology high resolution TEM (HRTEM) image of $PdSe_2$. Reproduced with permission from Ref. [58], © American Chemical Society 2019. (f) Experimental morphology TEM image of $PtTe_2$. Reproduced with permission from Ref. [98], © WILEY-VCH Verlag GmbH & Co. KGaA, Weinheim 2019.

Table 1 The different synthesis methods to prepare NMDs

Synthesis method	Material	Precursor	Carrier gas or vacuum degree (Torr)	Source temperature (°C)	Growth zone temperature (°C)	Substrate/solvent	Ref.
ME	PtS_2	PtS_2 crystal	/	/	/	SiO_2/Si	[83]
	PtS_2	PtS_2 crystal	/	/	/	Al_2O_3/Si	[112]
	PtS_2	PtS_2 crystal	/	/	/	SiO_2/Si	[61]
	$PtTe_2$	$PtTe_2$ crystal	/	/	/	SiO_2/Si	[98]
	$PtSe_2$	$PtSe_2$ crystal	/	/	/	SiO_2/Si	[62]
	$PtSe_2$	$PtSe_2$ crystal	/	/	/	SiO_2/Si	[51]
	$PdSe_2$	$PdSe_2$ crystal	/	/	/	SiO_2/Si	[58]
	$PdSe_2$	$PdSe_2$ crystal	/	/	/	SiO_2/Si	[113]
	$PdSe_2$	$PdSe_2$ crystal	/	/	/	SiO_2/Si	[114]
LPE	PtS_2	PtS_2 powder	/	/	/	N-Methyl-2-pyrrolidone (NMP)	[115]
	PtS_2	PtS_2 powder	/	/	/	NMP	[104]
	$PtTe_2$	$PtTe_2$ powder	/	/	/	Isopropyl alcohol (IPA)	[77]
	PdS_2	PdS_2 powder	/	/	/	IPA	[80]
CVT	PtS_2	Pt, S, P powder with a molar ratio of 1:3:1, weighing 1 g	10^{-5}	800	740	/	[61]
	PtS_2	Pt and S powder with a molar ratio of 1:5	10^{-6}	900	750	/	[112]
	$PtSe_2$	Pt, S, P, Se powder with a molar ratio of 1:3:1:2	10^{-6}	900	700	/	[62]
	$PtSe_2$	Pt, Se, P, S powder with a molar ratio of 1:2:1:3, weighing 700 mg and 35 mg of I	10^{-6}	900	700	/	[56]
One step CVD	$PtSe_2$	$PtCl_2$ and Se powder	/	/	/	SiO_2/Si	[56]
	$PtSe_2$	H_2PtCl_6 and Se	Low pressure	/	900	Sapphire	[52]
	$PdSe_2$	Pd powder and Se powder	Ar	/		SiO_2/Si	[116]
	$PdSe_2$	Pd powder and Se powder	Ar	/	800	SiO_2/Si	[86]
	$PdSe_2$	$PdCl_2$ and Se granules	Ar/H_2 (10:1)	/	/	sapphire	[81]
	$PdSe_2$	$PdCl_2$ and Se powder	Ar (85 SCCM) and H_2 (15 SCCM)	/	/	Au foil	[117]
	$PdSe_2$	Pd powder and Se powder	600 SCCM Ar	450	815	SiO_2/Si	[108]
Two step CVD	PtS_2	S powder and Pt film	60 SCCM Ar	130	600	SiO_2/Si	[118]
	PtS_2	S powder and Pt film	10 SCCM Ar	280	800	SiO_2/Si	[119]
	$PtSe_2$	Se powder and Pt film	60 SCCM Ar	130	450	SiO_2/Si	[118]
	$PtSe_2$	Se powder and Pt film	Ar	245	450	SiO_2/Si	[73]
	$PtSe_2$	Se powder and Pt film	N_2	221	650	Quartz/sapphire	[63]
	$PtSe_2$	Se powder and Pt film	Ar/H_2 (9:1)	220	400	SiO_2/Si	[120]
	$PtSe_2$	Se powder and Pt film	Ar /H_2 (9:1)	220	400	SiO_2/Si	[121]
	$PtSe_2$	Se powder and Pt film	H_2/Ar (1:9)	250	450	fused quartz	[122]
	$PtSe_2$	Se powder and Pt film	50 SCCM Ar	220	450	SiO_2/Si	[123]
	$PtSe_2$	Se powder and Pt film	50 SCCM Ar	220	450	SiO_2/Si	[124]
	$PtSe_2$	Se powder and Pt film	50 SCCM Ar	220	380	SiO_2/Si	[125]
	$PtSe_2$	Se powder and Pt film	50 SCCM Ar	220	380	Si	[126]
	$PtSe_2$	Se powder and Pt film	H_2/Ar (1:9)	220	400	SiO_2/Si	[64]
	$PtSe_2$	Se powder and Pt film	Ar	220	420	SiO_2/Si	[66]
	$PtSe_2$	Se powder and Pt film	Ar	220	420	SiO_2/Si	[127]
	$PdSe_2$	Se powder and Pd film	Ar	220	480	SiO_2/Si	[67]
	$PdSe_2$	Se powder and Pd film	Ar and H_2		357	SiO_2/Si	[128]

controllability of the number of layers and large area uniformity [101]. Moreover, considering the strong interlayer force of the material and the in-plane anisotropy, it is still a challenge to obtain a single layer using ME method [102].

(b) LPE

LPE is also commonly used to prepare 2D NMDs with high yield and suitable for mass production [26]. Wang et al. used NMP as a solvent and prepared a PtS_2 microflake solution using

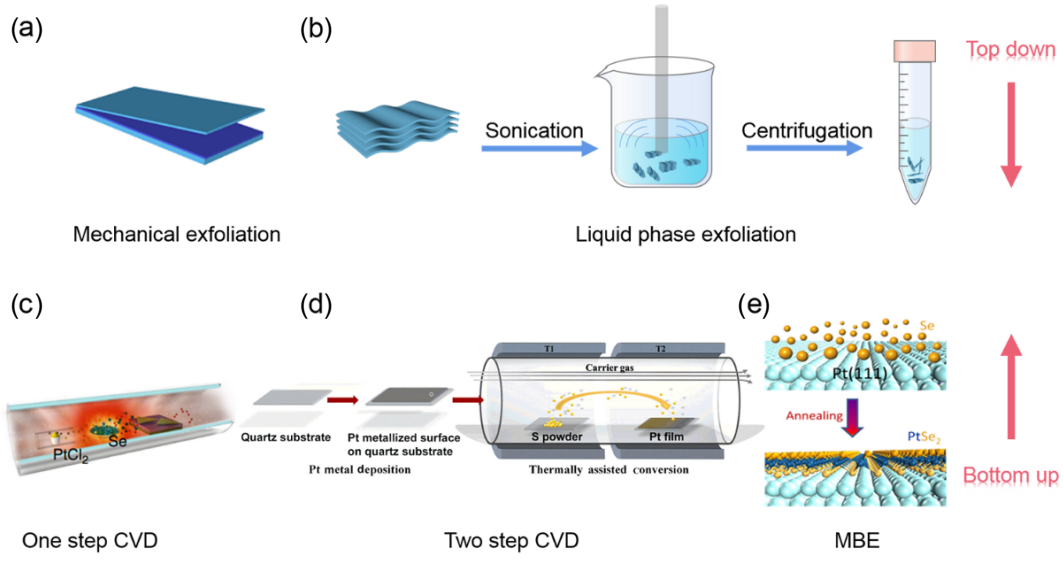

Figure 5 Schematic diagram of the synthesis method of 2D NMDs: (a) and (b) top-down fabrication; (c)–(e) bottom-up synthesis. (c) Reproduced with permission from Ref. [56], © Yu, X. C. et al. 2018. (d) Reproduced with permission from Ref. [103], © American Chemical Society 2019. (e) Reproduced with permission from Ref. [50], © American Chemical Society 2015.

probe sonication [104]. After sonication and concentration, the expected PtS_2 flakes with lateral dimensions of several microns and 0.35 μm thickness were fabricated with high yield. In another study, the $PtTe_2$ nanosheets were synthesized using the same cost-effective and facile method. Moreover, thanks to the suitable surface energy, IPA was chosen as an exfoliation solvent to prevent aggregation of flakes [77]. Therefore, the selection of appropriate solvent is very important for the LPE of 2D materials. According to the thermodynamics laws, choosing a solvent with a small difference in surface energy from the 2D material is conducive to LPE [105].

LPE method features some advantages, including facile preparation process and high yield production [26]. Compared to ME method, LPE method may be more suitable for applications that require a large amount of materials, such as electrochemical energy storage, catalysis, sensing, or composite fillers [8]. However, the LPE method also has some inevitable disadvantages, such as low single-layer yield, uncontrollable number of layers, and relatively small lateral dimensions [34].

3.2.2 *Bottom-up methods*

(a) One-step CVD

ME, LPE and vapor-phase growth are usually used to prepare 2D materials. ME can be used to prepare several 2D materials [106]. Although this method can produce high-quality 2D materials, it is not suitable for the large-scale production of 2D materials. The LPE method is suitable for the low-cost and mass production of 2D materials. Unfortunately, the unpredictable sizes and thicknesses and unexpected defects limit the wider application of 2D materials [107].

CVD is a scalable and controllable method to produce high-quality and large-area 2D materials [28]. The CVD synthesis approaches of NMDs can be categorized into one-step CVD method and two-step CVD method, as shown in Figs. 5(c) and 5(d). One-step preparation of NMDs comprises a direct reaction of a Pt/Pd source and chalcogenide enriched gas to form NMDs crystals on the substrates. Ma et al. synthesized $PdSe_2$ nanosheets by evaporating $PtCl_2$ and Se granules, followed by reaction and deposition on a sapphire substrate [81]. Gu et al. synthesized a few-layer (≥ 2 layers) $PdSe_2$ crystal on different substrates using CVD and revealed the effect of temperature on the shape of $PdSe_2$ [86]. They used DFT calculations and kinetic Wulff construction (KWC) modeling to explain the growth process and describe the morphology evolution of $PdSe_2$ crystals on SiO_2/Si substrates. The results show that growth temperature is a key factor of the $PdSe_2$ growth kinetics. The higher the substrate temperature, the faster the growth rate, and the larger and thicker the crystal. As shown in Fig. 6(a), by controlling the growth temperature, few-layer $PdSe_2$ crystals, with different morphologies (including "heart-like" and "square-like" shapes), were grown on a SiO_2/Si substrate. Interestingly, the growth shape of $PdSe_2$ depends on the different substrates. The "square-like" shapes can also be found on sapphire and mica substrates. However, the shape of $PdSe_2$, grown on Au foil, is irregular [86]. Xu et al. also synthesized $PdSe_2$ nanosheets using CVD [108]. They were able to tune the thickness, size, nucleation density and morphology of $PdSe_2$ nanosheets via the systematic regulation of temperature during the growth process. To compare the similarities and differences of NMDs for the one-step CVD growth process more intuitively, we summarize important growth data, as shown in Table 1.

The CVD method can provide a scalable and controllable way to produce high quality, high-performance and large-area nano-structured materials with a reasonable cost [28, 109]. Moreover, the number of layers, size, morphology and orientation of films grown by CVD can be controlled by changing the growth parameters such as temperature, pressure, flow rate of carrier gas, source–substrate distance, and relative amounts of source materials [28]. Therefore, the CVD method is very important for fundamental research and exploring the applications of 2D materials.

(b) Two-step CVD

The two-step CVD method is also called thermally assisted conversion (TAC). Metal or metal oxide is deposited on the substrate in advance, which then reacts with vapor phase chalcogen precursors in a quartz tube furnace and converted to the corresponding metal chalcogenide compound [103]. The main techniques used for precursor deposition are electron-beam evaporation, magnetron sputtering, and standard spin-coating methods. The size and thickness of the metal chalcogenide compound film mainly depend on the pre-deposited precursor film [110]. The TAC method was successfully used to synthesize ultrathin NMDs film on a large scale.

Zhan et al. synthesized single-layer and few-layer MoS_2 on SiO_2 substrates using TAC technology. Their results showed that the

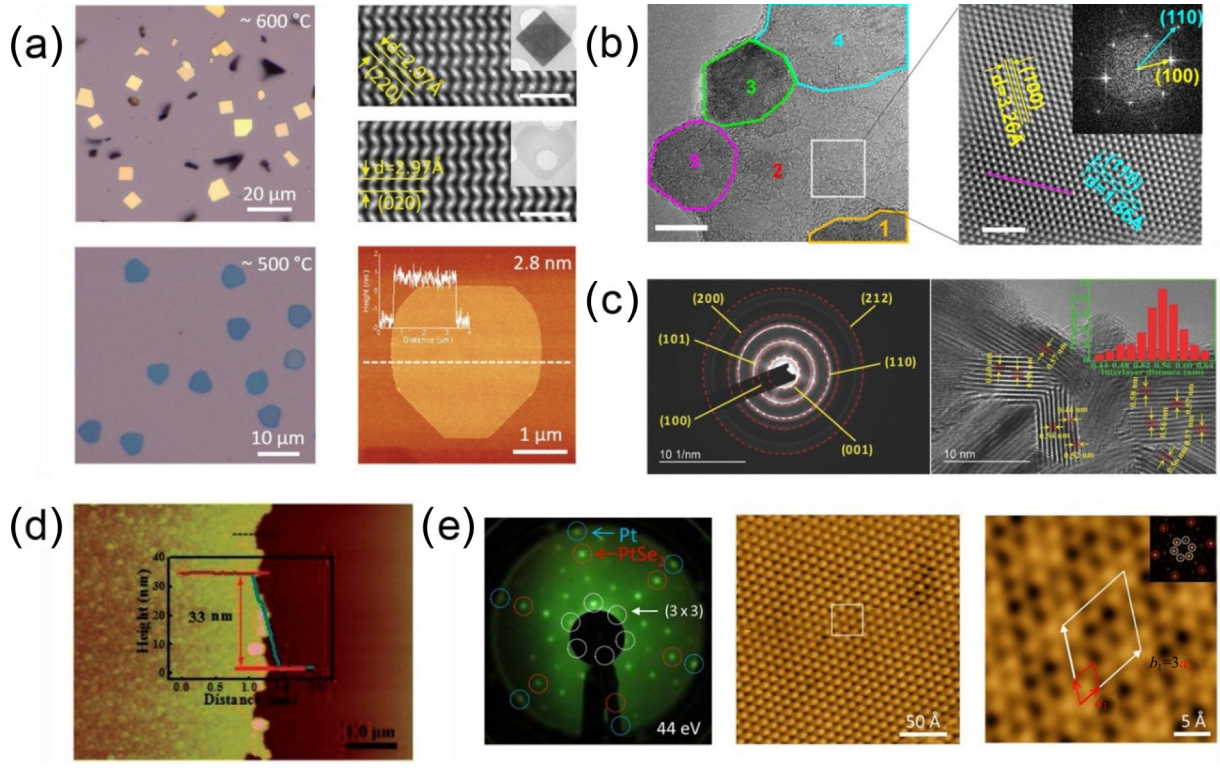

Figure 6 (a) Measured morphology (optical microscopy, high-angle annular dark-field scanning TEM (HAADF-STEM), and atomic force microscopy (AFM)) images of $PdSe_2$. Reproduced with permission from Ref. [86], © WILEY-VCH Verlag GmbH & Co. KGaA, Weinheim 2020. (b) Experimental morphology (TEM, HRTEM) images of $PtSe_2$. Reproduced with permission from Ref. [63], © WILEY-VCH Verlag GmbH & Co. KGaA, Weinheim 2019. (c) Experimental morphology (SAED, HRTEM) images of $PtSe_2$. Reproduced with permission from Ref. [66], © WILEY-VCH Verlag GmbH & Co. KGaA, Weinheim 2018. (d) Experimental morphology (AFM image, the inset shows the height profile) images of $PdSe_2$ film. Reproduced with permission from Ref. [128], © WILEY-VCH Verlag GmbH & Co. KGaA, Weinheim 2019. (e) Experimental morphology (LEED pattern and STM) images of $PtSe_2$ film. Reproduced with permission from Ref. [50], © American Chemical Society 2015.

size and thickness of the MoS_2 layer can be altered by changing the size of the substrate and the thickness of the pre-deposited Mo [111]. Recently, pre-deposited Pt and Pd metal layers, following selenization or sulfidation, were widely used to prepare 2D NMDs. We have summarized important date for the preparation of NMDs using TAC method (Table 1).

Jiang et al. proposed a transfer-free growth method for the preparation of $PtSe_2$ films. This method can be simply described as a metal mask to deposit the patterned Pt film. This metal mask can directly synthesize the patterned $PtSe_2$ structure without the need for transfer and etching. Using this method, the authors synthesized $PtSe_2$ thin films with different thicknesses (centimeters, and large areas) on different substrates such as silicon, quartz, and sapphire (Fig. 6(b)) [63]. Based on the crystallographic plane analysis, as-synthesized $PtSe_2$ has an octahedral 1T phase structure.

Zeng et al. also synthesized $PtSe_2$ using the TAC method (Fig. 6(c)). The group first used magnetron sputtering to deposit a 12 nm Pt film on SiO_2/Si substrate [66]. The polycrystalline film of $PtSe_2$, with a vertically aligned layered structure, can be observed using high-resolution TEM. Later, the wafer-scale $PdSe_2$ film was synthesized by the same team. The Pd metal layers were first deposited on SiO_2/Si, using magnetron sputtering. By controlling the thickness of the precursor Pd, 2D $PdSe_2$ with a thickness ranging from 1.2 nm to 20 nm, can be synthesized. In addition, an unexpected effect was observed. As the thickness increased, the Raman spectrum showed a significant red shift [67]. Luo et al. performed a synthesis using the TAC method. The 8 nm Pd film was deposited on a SiO_2/Si substrate using an electron beam evaporator (Fig. 6(d)) [128]. In addition, Zhang et al. found that the amount of Te flux would affect the final compound and obtained a PtTe phase [129]. TAC method can not only better control the uniformity and thickness of the film but also provide a facile strategy to directly prepare large-area controllable patterned 2D layered films on several substrates [67]. The good uniformity of the growth sample is mainly attributed to the excellent controllability of the deposition of the precursor film.

(c) MBE

MBE is a relatively new method for epitaxial film formation that uses special vacuum coating process.

As a member of NMDs, monolayer $PtSe_2$ was synthesized using a single step of direct selenization of a Pt(111) substrate via MBE. The growth of the single-layer $PtSe_2$ thin-film involved a simple precursor-free method, i.e., directly selenizing the Pt(111) substrate in a single step. As shown in Fig. 5(e), selenium atoms were deposited on a Pt(111) substrate, and then the sample was annealed at ~ 200 °C to obtain epitaxial $PtSe_2$ films (Fig. 6(e)) [50]. Yan et al. also successfully achieved epitaxial growth of high-quality $PtSe_2$ films using MBE [130]. The group showed that the thickness of $PtSe_2$ films can be controlled, and they found that $PtSe_2$ had a distinct tunable bandgap, using angle-resolved photoemission spectroscopy (ARPES). Recently, Xiong et al. reported electronic devices made from MBE-grown $PtSe_2$ and first reported metal oxide-silicon field effect transistors (MOSFETs) that were fabricated on $PtSe_2$ grown via MBE [131]. The MOSFETs, which were based on $PtSe_2$, showed interesting characteristics such as n-type conduction and ON/OFF ratios as high as 1,600. As for $PdTe_2$, Li et al. used MBE to synthesize $PtTe_2$ films, and they measured the band structure of 6-layer $PtTe_2$ films using ARPES [132]. Moreover, the air exposure experiments indicated that the $PtTe_2$ films had excellent chemical stability. Liu et al. also used a bottom-up method via MBE to grow $PdTe_2$ films on $SrTiO_3$(001) and investigated the electronic and superconducting properties of $PdTe_2$ [75]. Furthermore, Li et al.

reported the growth of bilayer $PdSe_2$ on a graphene-SiC(0001) substrate via MBE, and they found that the thickness of graphene affected the bandgap of $PdSe_2$ [133]. A bandgap shift of 0.2 eV can be observed in $PdSe_2$ layers grown on monolayer graphene, compared to those grown on bilayer graphene.

In addition to the above preparation methods, recently, a research team reported a novel method of synthesizing $PtTe_2$ from 2D Te deposited from Pt by laser irradiation [134]. The size and shape of the $PtTe_2$ synthesis area can be designed during the laser irradiation process. The authors studied the evolution of $PtTe_2$ synthesized under different 2D Te thicknesses, laser powers and exposure time. According to the experimental results, the best condition for laser-induced $PtTe_2$ is at a laser power of ~ 10 mW for 5 s. This novel growth method can be applied to $PtTe_2$ patterning directly on flexible substrates, which will help other applications of metallic noble TMDs in the future.

Compared with the CVD method, MBE allows for precise control of the growth rate of the film due to decoupling of the substrate temperature from the evaporation temperature of the growth precursor. MBE can offer significant advantages for better growth of highly uniform wafer-scale 2D TMDs films. It also enables high accuracy to control the growth temperature and precursor flux, while using a pollution-free environment [135].

Moreover, the ionic-intercalation method has the advantages of solution processability, mass production, and high yield of monolayers, which has been demonstrated for TMDCs such as MoS_2, WS_2, $MoSe_2$ and SnS_2 [136, 137]. Considering the mass production of 2D NMDs, the ionic specie intercalation method can be considered.

4 Applications of NMDs

4.1 Ultrafast photonics

A mode-locking technique, which is based on saturable absorbers (SAs), has turned out to be one of the most efficient techniques for ultrafast pulse generation. These laser systems can be used in areas such as laser surgery, ultrafine laser micromachining, high-accuracy measurements, and ultrafast pump sources [127]. In recent years, graphene [65], MXenes [138], TMDs (such as MoS_2 and WS_2) [139, 140], black phosphorus [141] and other 2D materials were included as members of a new SAs family. The bandgaps of TMDs are relatively large. For example, monolayer MoS_2 and monolayer WS_2 have bandgaps of 1.78 and 1.84 eV, respectively. With changing thickness, the tunable bandgap enables a strong resonance response of TMDs in the visible band [142]. Similarly, the layer-controlled band gap characteristics of NMDs make its broadband optical response potentially useful in optical applications, especially in the field of ultrafast optics. Therefore, some research groups already studied the nonlinear optical (NLO) properties of NMDs.

Wang et al. systematically revealed the excellent NLO performance and ultrafast dynamics of layered $PtSe_2$ (Fig. 7(a)) [122]. The group discussed the changes of nonlinear absorption and ultrafast carrier dynamics with increasing layer thickness. In addition, they proposed an optical nonlinear method to better understand the transition between semiconductor and semimetal. The results indicate that $PtSe_2$ is a promising candidate for nanophotonic devices such as saturable absorbers (SAs). Furthermore, NMDs have a narrow bandgap, ranging from 0.25 to 1.6 eV [62], which allows all photons in the fiber laser (photon energy 0.5–1 eV) to transition directly from the valence band to the conduction band. This results in a robustly saturated absorption and inherently stable mode-locked operation [73]. Considering the excellent saturable absorption, NMDs are ideal candidates for saturable absorbers for the generation of ultrashort pulses. Yuan et al. studied the nonlinear optical absorption characteristics of $PtSe_2$ at 1,064 nm, and their results showed that it exhibited typically saturated absorption [73]. They also showed that $PtSe_2$ film can be used as an efficient nonlinear absorption media to generate mode-locking pulses in a Yb-doped fiber laser (Fig. 7(b)). The mode-locked pulse centered at 1,064.47 nm has a pulse duration of 470 ps, a 3 dB spectral bandwidth of 2.0 nm, a repetition rate of 4.08 MHz, and a signal to noise ratio (SNR) of 53 dB (Fig. 7(b)). To investigate the long-term stability of the fiber lasers, the output spectra of the mode-locked dissipative soliton pulse were continuously monitored for 12 h. At about the same time, Long et al. used PtS_2 nanosheets to generate mode-locked ultrafast pulses [115]. The prepared PtS_2 SA was used in two different fiber laser systems (Er-doped fiber laser and Yb-doped fiber laser). The two laser systems produced mode-locking laser pulses at ~ 1.5 μm or ~ 1 μm, respectively. As members of NMDs, $PdSe_2$, PdS_2, and $PtTe_2$ were also found to be suitable for passive Q-switched laser applications. Furthermore, the $PdSe_2$ nanosheets were used as a SA in passively Q-switch laser devices. The Q-switched Nd:$GdLaNbO_4$/$PdSe_2$ laser yielded a 405 mW average output power for 8.8 W (absorbed pump power) at 879 nm [81].

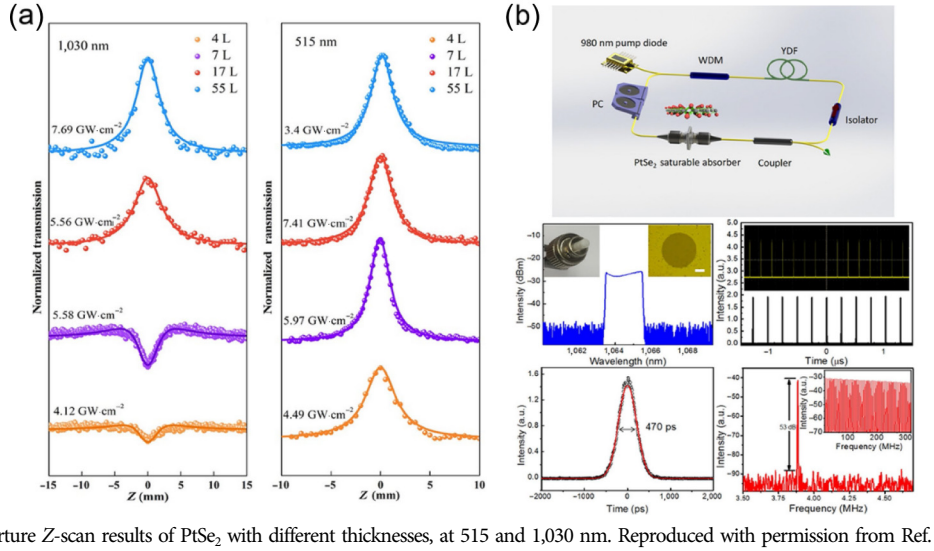

Figure 7 (a) Open-aperture *Z*-scan results of $PtSe_2$ with different thicknesses, at 515 and 1,030 nm. Reproduced with permission from Ref. [122], © WILEY-VCH Verlag GmbH & Co. KGaA, Weinheim 2019. (b) Experimental setup of the YDF laser ring cavity and laser mode-locking characteristics, using the $PtSe_2$ layer SA. Reproduced with permission from Ref. [73], © American Chemical Society 2018.

PdS_2 was first used to demonstrate stable Q-switched and mode-locked erbium-doped fiber lasers (EDFLs). Self-starting Q-switching operation at 1,567 nm was achieved with a threshold pump power of 50.6 mW. The achieved pulse duration of the mode-locked EDFL in this work was 803 fs, which indicates that PdS_2 SA is a promising candidate for 2D materials in NLO applications [80]. Cheng et al. successfully fabricated a SA using $PtTe_2$. The group also demonstrated passively Q-switched laser operation within a Yb-doped fiber laser cavity at 1,066 nm [77]. Recently, Liu et al. reported the giant nonlinear optical activity in 2D $PdSe_2$ [143]. They demonstrated that the $PdSe_2$ exhibited a unique thickness-dependent second harmonic generation (SHG) feature. That is, when the number of layers is odd, the second harmonic signal is weak; when the number of layers is even, the second harmonic signal is stronger. This phenomenon is just the opposite of that of other transition metal chalcogenides. Moreover, the $PdSe_2$ also has large two-photon absorption (TPA) coefficients and high modulation depths. Very recently, Han et al. [144] used a Fabry-Perot cavity with a 500 nm thick SiO_2 layer on a Si substrate to demonstrate the three-photon luminescence of the $PtSe_2$ atomic layers. Based on the three-photon emission of the $PtSe_2$ atomic layer, the authors demonstrated nonlinear optical encoding and encryption for secure information applications. This study is beneficial for exploring the mechanism of $PtSe_2$ nonlinear luminescence and provides a simple way for promoting $PtSe_2$ luminescence efficiency. In addition, this research will pave the way for integrated nonlinear optical devices.

To summarize, the band gap characteristics of NMDs enable all photons in fiber lasers to jump directly from the valence band to the conduction band [62, 73], which can produce powerful saturable absorption and stable mode-locking operation. In addition, in the application of ultrafast photonics, in order to obtain ultrashort pulses, array preparation or construction of heterojunctions can be considered to improve its saturation absorption characteristics.

4.2 Electronic devices

Thanks to their high carrier mobility, 2D layered materials may be used in the field of nanoelectronics, such as field-effect transistors (FETs). The performance of electronic devices is largely determined by carrier density and mobility. Since the discovery of graphene, TMDs, BP and other 2D materials have triggered extensive research due to their excellent properties [145, 146]. Being the most studied TMDs, MoS_2 is used to manufacture FETs. However, the mobility of FETs based on MoS_2 in practical applications is often an order of magnitude lower than the theoretically predicted value [147, 148]. Moreover, the FETs, which are based on TMDs, are only sensitive to visible light. Therefore, they are not useful for applications in the infrared [149]. The instability of BP in the air limits its application in optoelectronics [150]. However, it is still useful to search for emerging 2D materials with high ambient stability and good performance. NMDs provide both strong interlayer-coupling and a tunable bandgap [53, 83]. In addition, the theory predicts that NMDs have a high carrier mobility at room temperature, which exceeds 1000 $cm^2 \cdot V^{-1} \cdot s^{-1}$ [85]. As an excellent candidate for optoelectronic application, NMDs have drawn the attention of researchers worldwide.

Zhao et al. prepared a few-layer $PtSe_2$ FET and back-gated FET with bulk $PtSe_2$ (Fig. 8(a)) [62]. They found that, when the few-layer $PtSe_2$ FET exhibited semiconducting behavior with high room-temperature electron mobility (210 $cm^2 \cdot V^{-1} \cdot s^{-1}$), the bulk $PtSe_2$ device demonstrated metallic properties with high conductivity (6.20×10^5 $S \cdot m^{-1}$). Moreover, the 8-nm-thick $PtSe_2$ device showed that both the "on" state conductance and mobility showed temperature dependence. The "on" state conductance of the 8 nm $PtSe_2$ was 4.58×10^{-5} s at 300 K. However, when the temperature dropped to 50 K, the "on" state conductivity decreased to 1.1×10^{-5} s. The mobility of the 8 nm $PtSe_2$ reached 140 $cm^2 \cdot V^{-1} \cdot s^{-1}$, and when the temperature dropped to 125 and 25 K, the corresponding mobilities were 233 and 149 $cm^2 \cdot V^{-1} \cdot s^{-1}$. The change in mobility at higher temperatures is attributed to suppressed electron–phonon scattering, while the change at a lower temperature is mainly due to Coulomb scattering. In addition, the $PtSe_2$ devices show excellent ambient stability, which is better than other 2D materials such as BP. The intrinsic electric properties were investigated using typical output characteristics (source-drain current (I_{sd}) vs. drain bias (V_{sd})) at different temperatures by another group [63]. When the temperature decreased from 300 to 77 K, the I_{sd} also decreased. This indicates that $PtSe_2$ has semiconductor properties. The FET, which is based on $PtSe_2$, shows p-type unipolar operation, with a high field-effect hole mobility of 6.2 $cm^2 \cdot V^{-1} \cdot s^{-1}$ and an on-off ratio of 5×10^3.

As for PtS_2, Li et al. designed a FET, which was based on exfoliated PtS_2 flakes to study the electronic transport properties and potential applications of a few-layered PtS_2 [61]. Previous reports confirmed that h-BN can improve the mobility of graphene [151], MoS_2 [152] and black phosphorus [153]. To confirm whether h-BN was also effective for PtS_2, the authors prepared PtS_2 FETs on SiO_2 (denoted as PS) and on SiO_2-supported h-BN (denoted as PB). The results show that the field-effect mobility of the PB device was about 13 $cm^2 \cdot V^{-1} \cdot s^{-1}$, much higher than the PS device (< 1 $cm^2 \cdot V^{-1} \cdot s^{-1}$). Hence, it can be concluded that h-BN can also improve the performance of PtS_2 [61]. Moreover, the transfer curves (I_{ds}–V_g) of PS and PB devices also show improved performance for h-BN. Zhao et al. fabricated a FET, which was based on large-scale PtS_2 [119]. The transfer curves of PtS_2 FETs exhibited typical a p-type transport behavior. When the channel width increased from 10 to 30 μm, the FET's driving capability improved for a higher on-state current.

As an important member of NMDs, $PdSe_2$ also shows excellent photoelectric properties, and it has been extensively studied over the last years. Long et al. fabricated a FET, which was based on multilayer $PdSe_2$ flakes, using the conventional electron-beam lithography process (Fig. 8(b)) [58]. The performance of the $PdSe_2$ FET before and after annealing was compared. The results indicate that the annealing process can indeed improve the mobility. Before annealing, the maximum electron and hole mobilities were ~ 59.8 and 16.1 $cm^2 \cdot V^{-1} \cdot s^{-1}$, respectively, and the on/off ratio was ~ 10^2. After annealing, the electron and hole mobilities increased to ~ 138.9 and 57.0 $cm^2 \cdot V^{-1} \cdot s^{-1}$, respectively, and the on/off ratio was increased to 10^3. Moreover, the $PdSe_2$ FET device exhibited weak p-type conductivity and its optical response rate was as high as 42.1 $A \cdot W^{-1}$.

Gu et al. fabricated FET devices with eight electrodes using a back-gate configuration (Fig. 8(c)) [86]. The FET, which was based on few-layer $PdSe_2$, showed tunable bipolar charge carrier conduction with electron mobility reaching 294 $cm^2 \cdot V^{-1} \cdot s^{-1}$ and the on-off ration reached 10^3. The electric properties of 2D $PdSe_2$ depended on the thickness. When the thickness increased from 3.8 to 9 nm, the on/off ratio for electrons decreased from 10^4 to 10^2. Moreover, the anisotropic electric properties of $PdSe_2$ were studied using angle-resolved transport measurements. The results indicate that few-layer $PdSe_2$ has strong in-plane anisotropic optical properties. FETs, based on ultrathin $PdSe_2$, show intrinsic ambipolar characteristics, and the polarity of the FET could be tuned. Chow et al. characterized FETs, which used a back-gated configuration. They also introduced a simple vacuum annealing process to realize high-performance unipolar n-type $PdSe_2$ FET with mobilities reaching ≈ 216 $cm^2 \cdot V^{-1} \cdot s^{-1}$ and on/off ratio of 10^3

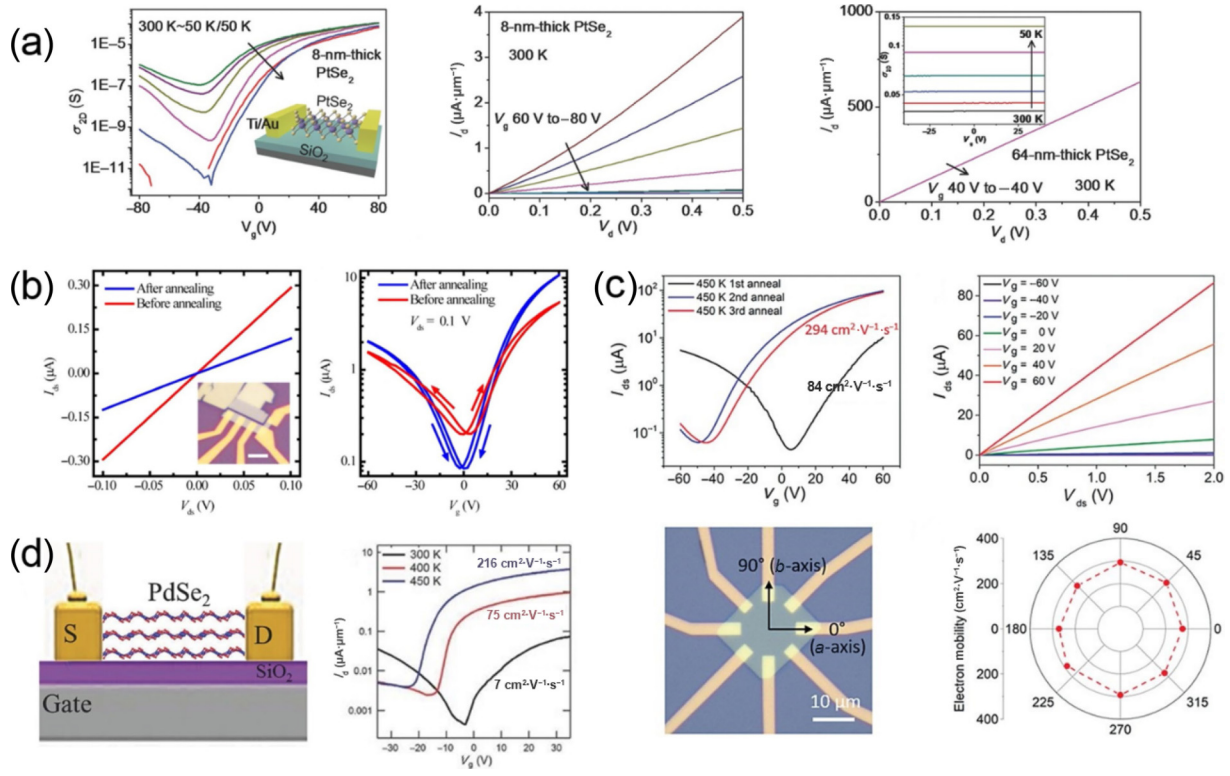

Figure 8 (a) Transfer-and output-curves of a $PtSe_2$ FET with different thicknesses. Reproduced with permission from Ref. [62], © WILEY-VCH Verlag GmbH & Co. KGaA, Weinheim 2016. (b) Transfer and output curves of a $PdSe_2$ FET before and after annealing. Reproduced with permission from Ref. [58], © American Chemical Society 2019. (c) Measurement results of an eight-electrode FET device. Reproduced with permission from Ref. [86], © WILEY-VCH Verlag GmbH & Co. KGaA, Weinheim 2020. (d) Schematic representation and transfer curves of a $PdSe_2$ FET. Reproduced with permission from Ref. [55], © WILEY-VCH Verlag GmbH & Co. KGaA, Weinheim 2017.

[55]. From the transfer curves, it can be seen that the threshold voltage gradually moved towards negative bias, which indicates that the Fermi level moves toward the conduction band of $PdSe_2$. This indicates that the annealing process can remove surface adsorbates, and a high-performance unipolar n-type $PdSe_2$ FET can be realized (Fig. 8(d)).

NMDs have unique layer-related characteristics, high carrier mobility, and good stability, which make them attractive in the field of FET. In order to improve the performance of FET based on NMDs, there are several ways to try to increase their carrier mobility: 1. to explore different substrates and find the most suitable substrate to improve contact and reduce scattering of impurities [61]; 2. to change the number of layers of NMDs and find the best number of layers. 3. to construct a heterojunction based on NMDs.

4.3 Photoelectronic devices

A long-wavelength infrared photodetector has wide applications in many areas such as remote sensing, thermal imaging, biomedical optics, optical communication, industrial automation, and medical imaging [58, 154]. Mid-infrared detection, however, using 2D materials has always been a challenging task [155].

Recently, NMDs with a tunable bandgap, high carrier-mobility, and excellent environmental stability showed a promising potential for optoelectronic applications. For example, $PtSe_2$ shows the highest mobility in NMDs, which is comparable to black phosphorus, and the bandgap ranges from 0 to 1.2 eV [63]. Therefore, the optical response band would cover even the mid-infrared region. Yu et al. studied bilayer $PtSe_2$. They found that when combined with defect modulation, $PtSe_2$ showed strong light absorption in the mid-infrared region. And they built a broadband mid-infrared photodetector that was operating at room temperature. Both the responsivity and response speed far exceeded those of the recently discovered black AsP in the 3–5 μm range (Fig. 3(c)) [56, 156]. Zeng et al, reported a high-performance, air-stable, self-powered, and broadband photodetector based on a vertically aligned $PtSe_2$-GaAs heterojunction [66]. The photodetector showed a broadband sensitivity, ranging from DUV to near-infrared, and the peak light sensitivity ranged from 650 to 810 nm at zero bias voltage. Interestingly, the prepared heterojunction showed a typical rectification behavior even in the absence of light. The optoelectronic analysis showed that the I_{on}/I_{off} ratio, responsivity, specific detectivity, and the response speed of the photodetector were 3×10^4, 262 mA·W^{-1}, 2.52×10^{12} Jones, and 5.5/6.5 μs, respectively. These numbers are comparable to or better than those of other TMDs photodetectors. In addition, the $PtSe_2$/GaAs heterojunction can be used as a self-driven photodetector under different light intensities. Furthermore, $PtSe_2$/GaAs devices can be switched between on and off states with good reproducibility (Fig. 9(a)). The stability test results indicate that this heterojunction photodetector has high stability in air (Fig. 9(b)) [66].

As mentioned above, both the monolayer and bulk PtS_2 are indirect bandgap semiconductors. Thus, PtS_2 is naturally a promising candidate for broadband photodetectors. Wang et al. published a broadband photodetector based on 2D PtS_2 [112]. The photodetector had a photoresponse ranging from visible to mid-infrared. At the near-infrared (830 nm), the photodetector exhibited fast photoresponse time (175 μs).

For $PdSe_2$, the bandgap can be reduced from 1.3 eV for a monolayer to 0 eV for the bulk material. Hence, the device based on $PdSe_2$ can extend the detection range from the visible to the near-infrared and mid-infrared regions.

Liang et al. reported a high-performance broadband $PdSe_2$-based photodetector [79]. Based on the $PdSe_2$-gated photodetector, the group found the gate-tunable photoresponsivity. This gate photodetector not only had an excellent photoelectric performance in the visible and near-

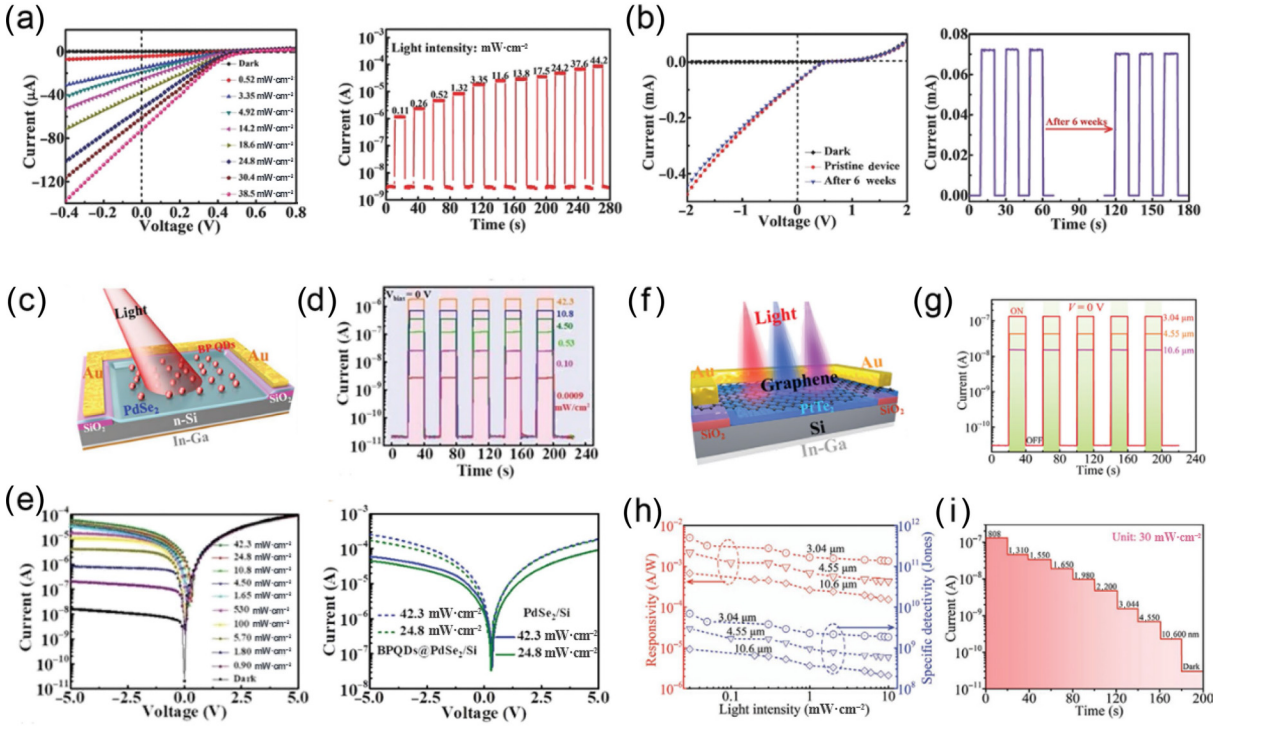

Figure 9 Application of NMDs in photodetectors. (a) and (b) A photodetector based on $PtSe_2$/GaAs heterojunction. Reproduced with permission from Ref. [66]. © WILEY-VCH Verlag GmbH & Co. KGaA, Weinheim 2018. (c)–(e) A photodetector based on $PdSe_2$/Si heterojunction. Reproduced with permission from Ref. [67]. © WILEY-VCH Verlag GmbH & Co. KGaA, Weinheim 2018. (f)–(i) A photodetector based on $PtTe_2$/Si Schottky junction. Reproduced with permission from Ref. [157], © WILEY-VCH GmbH 2020.

infrared regions but it also featured high photoresponsivity in the mid-infrared region (up to 4.05 μm). In addition, the gate-tunable photoresponsivity offers more opportunities to control the performance of the phototransistor. Moreover, because $PdSe_2$ is anisotropic, the group also found that the photoresponse of the $PdSe_2$-based photodetector can be changed using the polarization angle of incident light [79]. These results confirm that $PdSe_2$ is a promising candidate material for infrared optoelectronics and perhaps other novel devices. Luo et al. developed a sensitive infrared photodetector (IRPD) that consisted of a germanium nanocone (GeNCs) array and a $PdSe_2$ multilayer [128]. The IRPD exhibits a clear photovoltaic behavior up to 1,550 nm, which renders the IRPD a self-driven device that needs no external power supply. The specific detectivity at 1,550 nm is 1.45×10^{11} Jones. The $PdSe_2$/GeNC array device has good sensitivity at 1,350, 1,550, 1,650, and even 2,200 nm, with good reproducibility. Moreover, they showed that the $PdSe_2$/GeNC can reliably record simple infrared images. Zeng et al. used TAC technology to synthesize a 2D $PdSe_2$ thin film at the wafer level and combined it with Si to prepare a photodetector (Fig. 9(c)) [67]. The $PdSe_2$/Si heterojunction photodetector has a high on/off ratio (≈ 10^5) (Fig. 9(d)), a high responsivity (300.2 mA·W^{-1}), and excellent specific detectivity (≈ 10^{13} Jones). To further optimize the photoresponse of the heterojunction, black phosphorous quantum dots (BPQDs) were used to modify the $PdSe_2$/Si heterojunction photodiode. Compared with the result of the *I*–*V* curve, it can be seen that the photocurrent of BPQDs@$PdSe_2$/Si has increased after modification of the BPQDs. This can be attributed to enhanced optical absorption (Fig. 9(e)). Moreover, the BPQDs@$PdSe_2$/Si heterojunction not only shows high sensitivity to different wavelengths, but also exhibits a fairly fast response speed. The response speed is comparable to those of photodetectors based on other TMDs [67, 158, 159]. Wu et al. demonstrated a photodetector that was based on a graphene/$PdSe_2$/germanium (Gr/$PdSe_2$/Ge) heterojunction [57]. The photodetector, which is based on the heterojunction, performs very well, with a high photoresponsivity, a high specific detectivity, a fast response speed, and broadband photosensitivity that ranges from DUV to MIR. The peak optical response of the Gr/$PdSe_2$/Ge heterojunction device is between 600 and 1,850 nm, which is consistent with the UV–Vis–IR absorption spectrum of the $PdSe_2$/Ge hybrid system. Moreover, the group also demonstrated high-resolution polarization imaging based on the heterojunction device. Their results show that the Gr/$PdSe_2$/Ge heterojunction has potential in polarization-sensitive broadband photodetection and imaging.

Recently, Zeng et al. reported van-der-Waals (vdW) epitaxial growth of a wafer-scale 2D platinum ditelluride ($PtTe_2$) layer. This was done by directly growing 2D $PtTe_2$ on n-Si to fabricate a high-quality $PtTe_2$/Si vertical Schottky junction photodetector (Fig. 9(f)) [157]. This photodetector shows a superior device performance. It features fast speed, a large bandwidth, and an excellent infrared imaging capability. Figure 9(g) shows the temporal photovoltaic response of the device to 3.04, 4.55, and 10.6 μm illumination. It can be clearly seen that the photodetector could be reversibly switched with good stability and reproductivity, yielding a high on/off ratio of ≈ 10^2–10^3. The responsivity and specific detectivity of $PtTe_2$/Si photodetector are higher than those of other MIR photodetectors (Fig. 9(h)). Moreover, the device also shows a remarkable good photovoltaic response in the near-infrared spectral bands (Fig. 9(i)).

In summary, the layer-dependent band gap characteristics of NMDs make them excellent channel materials for broadband detection from DUV to MIR, and it plays an important role in optical interconnection, such as light-wave communication and high-resolution imaging [160]. Overall, 2D NMDs have application prospects in the field of high-performance high-polarization-sensitive, broadband and air-stabilized photodetectors.

4.4 Meta optics

Over the past few decades, the development of flat optics has

brought interesting applications such as meta-surfaces, color prints, and meta-lenses. Although graphene and other 2D materials with excellent optical properties have been used in flat optics, the conventional phase-modulation mechanism still has some defects. Therefore, the field of meta optics still needs further exploration. 2D NMDs are believed to possess an unusual potential with respect to flat optics application, mainly because of their environmental stability and high refractive index.

Recently, Wang et al. demonstrated atomically thin high-performance meta-optics including a hologram and a meta-lens. In this new study, 4.3 nm thick $PtSe_2$ was synthesized via the TAC approach on a SiO_2/Si substrate. Direct laser writing (DLW) technology was explored to construct a predesigned phase-distribution on the $PtSe_2/SiO_2$/Si structure. The schematic diagram of the DLW is depicted in Fig. 10(a). The losses of atomically thin $PtSe_2$ nanosheets and the resonator structure were thoughtfully designed to achieve singular phase properties with a remarkable π-phase jump. Figure 10(b) shows a schematic diagram for binary meta-optics units. Thanks to the nontrivial singular phase properties, an angle-robust and high unit thickness diffraction efficiency of 0.96%·nm^{-1} for the visible frequencies were found. This showed significant superiority over the control group, for which a conventional phase regulation mechanism was used (Fig. 10(c)). Furthermore, the authors also revealed binary meta-optics-enabled Fresnel zone plate (FZP) lenses at visible frequencies. Diffraction limited focusing was achieved for visible frequencies (Fig. 10(d)). This timely approach expands the research of NMDs to an active and cutting-edge flat optics field [69].

4.5 Other applications

The thickness-related semimetal-to-semiconductor transition properties of NMDs make them potential candidates for optoelectronic device applications. We summarize applications of NMDs in ultrafast photonics, FET, photodetectors, and flat optics, but the application areas of NMDs are not limited to these fields.

NMDs have also shown their potential in other application areas such as gas sensors, electromechanical piezoresistive sensors, photocatalysis, all-optical modulator, and superconductors. The related applications of NMDs are summarized in Table 2. A $PtSe_2$ thin film, grown using TAC technology, was shown to have many potential applications in the field of high-performance gas sensing, with extremely short response and recovery time. The gas sensor with a $PtSe_2$ channel showed ultrahigh sensitivity to NO_2 at room temperature (Fig. 11(a)) [64]. An integrated nanoelectromechanical system (NEMS) piezoresistive pressure-sensor, which is based on freestanding PMMA/$PtSe_2$ membrane, exhibits very high sensitivity. It performs at least 82 times better than piezoresistive pressure-sensors based on other materials (Fig. 11(b)) [72]. Wang et al. used a methylene-blue photodegradation experiment to evaluate the photocatalytic activity of monolayer $PtSe_2$ film, and the results showed that $PtSe_2$ was a promising photocatalyst (Fig. 11(c)) [50]. Wei et al. proposed an all-optical modulator with a 2D $PtSe_2$-on-silicon structure [179]. Their results showed that the $PtSe_2$-based device was a potential choice for all-optical signal processing. Moreover, Chen et al. also demonstrated that $PtSe_2$ can be used as the catalyst for photoelectrochemical hydrogen production [180]. Kireev et al. reported an interesting work that $PtSe_2$ and $PtTe_2$ can be used for electronic tattoos [181]. The electronic tattoos based on $PtSe_2$ and $PtTe_2$ can be used for monitoring human physiological vital signs, such as the electrical activity of the heart and the brain, muscle contractions, eye movements, and temperature. Among them, $PtTe_2$ is considered to be the most suitable material due to its metallic structural characteristics. The $PtTe_2$ electronic tattoo performs better than gold and graphene electronic tattoos and it is comparable to medical-grade Ag/AgCl gel electrodes. Recently, Jiao et al. [182] designed a simple method to activate the 2D $PtSe_2$ basal plane through gentle Ar plasma treatment, while introducing Se, Pt atomic vacancies and Pt clusters, and achieved a high-efficiency hydrogen evolution reaction (HER). This study proves the great potential of activated 2D $PtSe_2$ as a HER ultra-thin catalyst and provides new insights for the rational design of 2D electrocatalysts.

5 Conclusion and prospects

In recent decades, NMDs has become highly popular research topics due to their unique structure, excellent optical and electrical properties, and environmental stability. This review systematically summarizes the fundamental properties (structural, electronic, optical, magnetic) of NMDs and preparation methods (CVT, ME, LPE, one-step CVD, two-step CVD, and MBE) of NMDs. Through our summary of the preparation methods, we find that TAC technology is already widely used in the preparation of NMDs. This is because, compared to other methods, TAC technology has the following advantages: (1) potential scalability, compatibility with standard process flows; (2) TAC can better

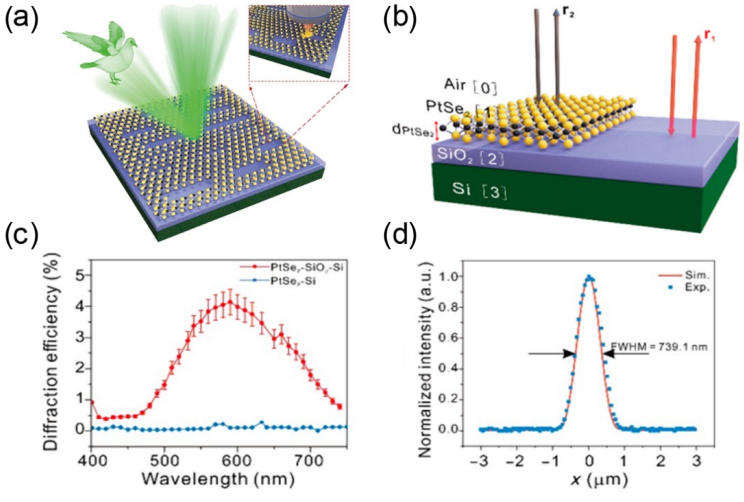

Figure 10 (a) Illustration of a laser-scribed binary meta-hologram. (b) Configuration of nanometric $PtSe_2$ layers placed on a uniform substrate, exhibiting an abrupt Heaviside phase shift nearby the critical coupling point. (c) Comparison of measured diffraction efficiencies for samples with and without the 290 nm thick silica layer. (d) Cross section of the simulated and experimental intensity distribution of the focal spot at the wavelength of 590 nm. (a)–(d) Reproduced with permission from Ref. [69], © American Chemical Society 2020.

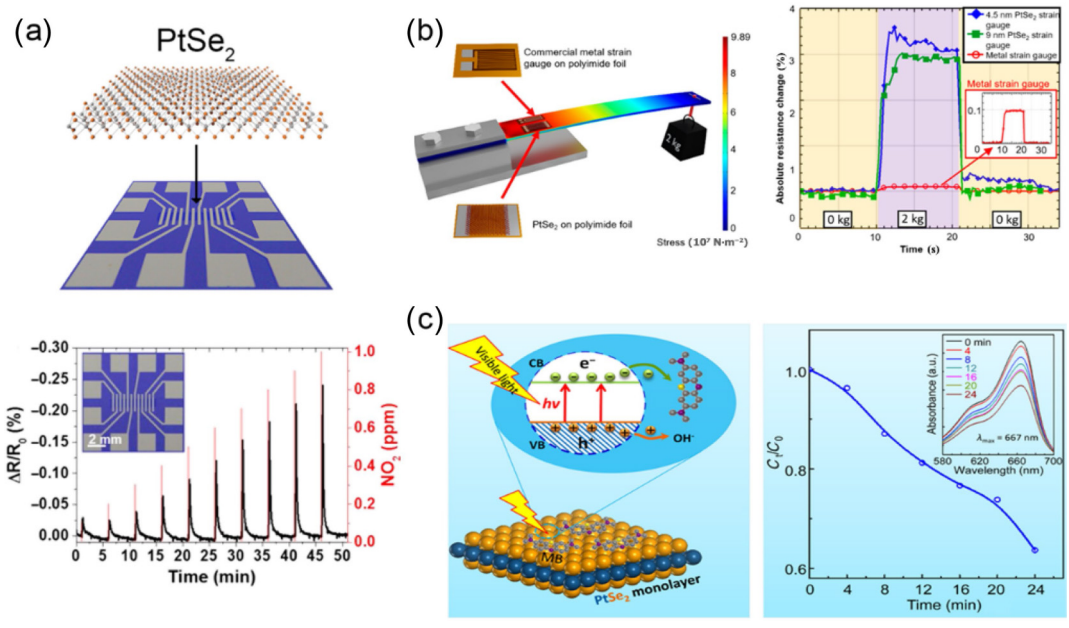

Figure 11 (a) Gas sensor based on a $PtSe_2$ film. Reproduced with permission from Ref. [64], © American Chemical Society 2016. (b) Electromechanical piezoresistive pressure sensors. Reproduced with permission from Ref. [72], © American Chemical Society 2018. (c) Photocatalytic activity of a single-layer $PtSe_2$ film. Reproduced with permission from Ref. [50], © American Chemical Society 2015.

Table 2 The applications of NMDs

Application	Material	Highlight	Refs.
Ultrafast Photonics	PtS_2	Wavelength 1,572 nm, pulse duration 2.064 ps, repetition rate 15.04 MHz, and output 1.1 mW; wavelength 1,568.8 nm, pulse duration 4.2 μs, repetition rate 24.6 kHz, and output 1.1 mW	[115, 104]
	$PtTe_2$	Wavelength 1,066 nm, pulse duration 5.2 μs, repetition rate 33.5 kHz, and output 2.48 mW	[77]
	$PtSe_2$	Wavelength range from visible light to near-infrared, pulse duration from tens of nanosecond (ns) to hundreds of picosecond (ps), repetition rate from tens of kHz to several GHz, output power range from a few milliwatts (mW) to more than one thousand milliwatts (mW)	[73, 161, 162, 127, 163, 164, 165]
	PdS_2	Wavelength 1565.8 nm, pulse duration 803 fs, repetition rate 12.1 MHz, and output 0.55 mW	[80]
	$PdSe_2$	Wavelength in the near infrared region, pulse duration in the hundreds of nanoseconds to hundreds of femtoseconds, repetition rate from more than one hundred kHz to ten MHz, and output power from a few tenths of a milliwatt to a few hundred milliwatts	[166, 81, 167, 168]
FET	PtS_2	Excellent electronic mobility (62.5 $cm^2 \cdot V^{-1} \cdot s^{-1}$), and bulk devices show metallic-like behavior, and ultrahigh on/off ratio (over 10^6)	[83, 112, 119]
	$PtSe_2$	Few-layer $PtSe_2$ FET exhibits semiconducting behavior and while bulk $PtSe_2$ device exhibits metallic-like behavior	[62, 63, 52, 169, 51, 131, 100, 170, 120, 121, 121]
	$PdSe_2$	Tunable ambipolar charge carrier conduction, high mobility (294 $cm^2 \cdot V^{-1} \cdot s^{-1}$), and high current on/off ratio (over 10^6)	[86, 55, 171, 172, 54, 108, 173]
Photodetector	PtS_2	Broadband photodetection from visible to mid-infrared, and a fast photoresponse time of 175 μs at 800 nm illumination	[112, 118, 61, 174]
	$PtTe_2$	THz photodetector, high photoresponsivity (1.6 $A \cdot W^{-1}$ without bias voltage)	[98]
	$PtSe_2$	Broadband sensitivity from deep ultraviolet to the mid-infrared range, good photoresponsivity (262 $mA \cdot W^{-1}$), and high specific detectivity (3.8×10^{14} Jones)	[66, 56, 123, 169, 124, 125, 175, 118, 126, 176, 177]
	$PdSe_2$	Highly sensitive, air-stable, high photoresponsivity (1.24×10^5 $A \cdot W^{-1}$), broadband ranging from DUV to MIR, and fast response speed (< 11 ms)	[58, 57, 67, 154, 79, 114, 108]
Meta optics	$PtSe_2$	Singular phase behavior, remarkable π phase jump	[69]
Gas sensor	$PtSe_2$	This gas sensor shows ultrahigh sensitivity to NO_2 gas with fast response time	[64]
Pressure sensor	$PtSe_2$	High negative gauge factors (up to −84.8), and high sensitivity (1.64×10^{-3} $mbar^{-1}$)	[72]
Catalytic	$PtSe_2$	The photocatalytic activity demonstrates that $PtSe_2$ is a promising photocatalyst	[50]
	$PdSe_2$	$PdSe_2$ can be used as an efcient electrocatalyst for hydrogen evolution reaction in an alkaline electrolyte, and both Pd and Se atoms exhibit high activity for hydrogen evolution	[178]
Magnetism	$PtSe_2$	Thickness-dependent localized magnetic moments induced by Pt-vacancy defects	[71]

control the uniformity and thickness of the film. Furthermore, TAC also provides a simple stage to directly prepare large-area controllable patterns using 2D-layered film on several substrates. We also summarize the recent applications of NMDs in ultrafast optics, FETs, photodetectors, meta optics, and other applications. Although progress has been made in certain areas in the past few years, there are still some areas where more in-depth knowledge would be desirable.

The two-step CVD method, which is widely used in preparing NMDs, has some advantages over other methods. But there are still some challenges, including the inability to develop large-scale and high-quality film samples to meet the needs of

industrialization. Therefore, further improvement of the synthesis method is necessary to obtain high-quality samples.

Many studies were done to explore the properties and applications of NMDs. Nevertheless, most of the reports focused on the popular members of NMDs such as $PtSe_2$ or $PdSe_2$. The promising potential of other members are not be explored much. For example, for the ultrafast photonics of NMDs, only $PtSe_2$ was widely reported, and there are few reports of other members of the NMDs class. Moreover, the research of ultrafast photonics with NMDs was not exhaustive enough, and most studies were limited to the study of nonlinear absorption properties. In other words, it would be very desirable if the ultrafast optical properties of other NMDs members were studied systematically and in more depth.

In general, NMDs have excellent photoelectric and magnetic properties. In terms of applications, those unique and excellent electronic properties would endow NMDs-based electronic devices with high performance. For example, there have been many studies focused on optoelectronic devices such as FET and photodetectors. However, there are few studies on magnetic applications and other aspects. Therefore, the exploration of NMDs in other application areas could be implemented in the future. For example, NMDs have environmental stability and high refractive index, so they have application prospects on meta-surfaces [69]. In addition, we believe that there are potential applications in the field of laser processing [69] and wearable bioelectronic applications [181].

Overall, considering the current stage of 2D NMDs, the challenges and opportunities in the near future are as follows: exploration of new technologies with the aim for mass production of high-quality 2D NMDs; study of a wider range of NMDs; discovery of novel applications and perhaps new emerging phenomenon.

Acknowledgments

The authors are grateful for the financial support from the National Natural Science Foundation of China (Nos. 61874141 and 11904239).

References

[1] Zhang, H. Ultrathin two-dimensional nanomaterials. *ACS Nano* **2015**, *9*, 9451–9469.

[2] Wang, Y. W.; Qiu, M.; Won, M.; Jung, E.; Fan, T. J.; Xie, N.; Chi, S. G.; Zhang, H.; Kim, J. S. Emerging 2D material-based nanocarrier for cancer therapy beyond graphene. *Coord. Chem. Rev.* **2019**, *400*, 213041.

[3] Tan, C. L.; Cao, X. H.; Wu, X. J.; He, Q. Y.; Yang, J.; Zhang, X.; Chen, J. Z.; Zhao, W.; Han, S. K.; Nam, G. H. et al. Recent advances in ultrathin two-dimensional nanomaterials. *Chem. Rev.* **2017**, *117*, 6225–6331.

[4] Miró, P.; Audiffred, M.; Heine, T. An atlas of two-dimensional materials. *Chem. Soc. Rev.* **2014**, *43*, 6537–6554.

[5] Xia, F. N.; Wang, H.; Xiao, D.; Dubey, M.; Ramasubramaniam, A. Two-dimensional material nanophotonics. *Nat. Photonics* **2014**, *8*, 899–907.

[6] Zeng, H. L.; Cui, X. D. An optical spectroscopic study on two-dimensional group-VI transition metal dichalcogenides. *Chem. Soc. Rev.* **2015**, *44*, 2629–2642.

[7] Kong, X. K.; Liu, Q. C.; Zhang, C. L.; Peng, Z. M.; Chen, Q. W. Elemental two-dimensional nanosheets beyond graphene. *Chem. Soc. Rev.* **2017**, *46*, 2127–2157.

[8] Chhowalla, M.; Shin, H. S.; Eda, G.; Li, L. J.; Loh, K. P.; Zhang, H. The chemistry of two-dimensional layered transition metal dichalcogenide nanosheets. *Nat. Chem.* **2013**, *5*, 263–275.

[9] Wang, Y. H.; Nie, Z. H.; Wang, F. Q. Modulation of photocarrier relaxation dynamics in two-dimensional semiconductors. *Light:Sci. Appl.* **2020**, *9*, 192.

[10] Agarwal, V.; Chatterjee, K. Recent advances in the field of transition metal dichalcogenides for biomedical applications. *Nanoscale* **2018**, *10*, 16365–16397.

[11] Zhang, S. L.; Guo, S. Y.; Chen, Z. F.; Wang, Y. L.; Gao, H. J.; Gómez-Herrero, J.; Ares, P.; Zamora, F.; Zhu, Z.; Zeng, H. B. Recent progress in 2D group-VA semiconductors: From theory to experiment. *Chem. Soc. Rev.* **2018**, *47*, 982–1021.

[12] Qiao, J. S.; Kong, X. H.; Hu, Z. X.; Yang, F.; Ji, W. High-mobility transport anisotropy and linear dichroism in few-layer black phosphorus. *Nat. Commun.* **2014**, *5*, 4475.

[13] Zhao, A. L.; Li, H.; Hu, X. J.; Wang, C.; Zhang, H.; Lu, J. G.; Ruan, S. C.; Zeng, Y. J. Review of 2D group VA material-based heterostructures. *J. Phys. D:Appl. Phys.* **2020**, *53*, 293002.

[14] Rodenas, T.; Luz, I.; Prieto, G.; Seoane, B.; Miro, H.; Corma, A.; Kapteijn, F.; Llabres i Xamena, F. X.; Gascon, J. Metal-organic framework nanosheets in polymer composite materials for gas separation. *Nat. Mater.* **2015**, *14*, 48–55.

[15] Zhao, M. T.; Huang, Y.; Peng, Y. W.; Huang, Z. Q.; Ma, Q. L.; Zhang, H. Two-dimensional metal-organic framework nanosheets: Synthesis and applications. *Chem. Soc. Rev.* **2018**, *47*, 6267–6295.

[16] Yamamoto, K.; Sakata, Y.; Nohara, Y.; Takahashi, Y.; Tatsumi, T. Organic-inorganic hybrid zeolites containing organic frameworks. *Science* **2003**, *300*, 470–472.

[17] Deng, H. X.; Doonan, C. J.; Furukawa, H.; Ferreira, R. B.; Towne, J.; Knobler, C. B.; Wang, B.; Yaghi, O. M. Multiple functional groups of varying ratios in metal-organic frameworks. *Science* **2010**, *327*, 846–850.

[18] Anasori, B.; Lukatskaya, M. R.; Gogotsi, Y. 2D metal carbides and nitrides (MXenes) for energy storage. *Nat. Rev. Mater.* **2017**, *2*, 16098.

[19] Shahzad, F.; Iqbal, A.; Kim, H.; Koo, C. M. 2D transition metal carbides (MXenes): Applications as an electrically conducting material. *Adv. Mater.* **2020**, *32*, 2002159.

[20] Jhon, Y. I.; Jhon, Y. M.; Lee, J. H. Nonlinear optics of MXene in laser technologies. *J. Phys. Mater.* **2020**, *3*, 032004.

[21] Wang, Y. F.; Xu, Y. H.; Hu, M. L.; Ling, H.; Zhu, X. MXenes: Focus on optical and electronic properties and corresponding applications. *Nanophotonics* **2020**, *9*, 1601–1620.

[22] Lei, J. C.; Zhang, X.; Zhou, Z. Recent advances in MXene: Preparation, properties, and applications. *Front. Phys.* **2015**, *10*, 276–286.

[23] Novoselov, K. S.; Fal′ko, V. I.; Colombo, L.; Gellert, P. R.; Schwab, M. G.; Kim, K. A roadmap for graphene. *Nature* **2012**, *490*, 192–200.

[24] Wang, Q. H.; Kalantar-Zadeh, K.; Kis, A.; Coleman, J. N.; Strano, M. S. Electronics and optoelectronics of two-dimensional transition metal dichalcogenides. *Nat. Nanotechnol.* **2012**, *7*, 699–712.

[25] Long, M. S.; Gao, A. Y.; Wang, P.; Xia, H.; Ott, C.; Pan, C.; Fu, Y. J.; Liu, E. F.; Chen, X. S.; Lu, W. et al. Room temperature high-detectivity mid-infrared photodetectors based on black arsenic phosphorus. *Sci. Adv.* **2017**, *3*, e1700589.

[26] Coleman, J. N.; Lotya, M.; O'Neill, A.; Bergin, S. D.; King, P. J.; Khan, U.; Young, K.; Gaucher, A.; De, S.; Smith, R. J. et al. Two-dimensional nanosheets produced by liquid exfoliation of layered materials. *Science* **2011**, *331*, 568–571.

[27] Güler, Ö.; Tekeli, M.; Taşkin, M.; Güler, S. H.; Yahia, I. S. The production of graphene by direct liquid phase exfoliation of graphite at moderate sonication power by using low boiling liquid media: The effect of liquid media on yield and optimization. *Ceram. Int.* **2021**, *47*, 521–533.

[28] Cai, Z. Y.; Liu, B. L.; Zou, X. L.; Cheng, H. M. Chemical vapor deposition growth and applications of two-dimensional materials and their heterostructures. *Chem. Rev.* **2018**, *118*, 6091–6133.

[29] Zheng, H. M.; Smith, R. K.; Jun, Y. W.; Kisielowski, C.; Dahmen, U.; Alivisatos, A. P. Observation of single colloidal platinum nanocrystal growth trajectories. *Science* **2009**, *324*, 1309–1312.

[30] Najmaei, S.; Liu, Z.; Zhou, W.; Zou, X. L.; Shi, G.; Lei, S. D.; Yakobson, B. I.; Idrobo, J. C.; Ajayan, P. M.; Lou, J. Vapour phase growth and grain boundary structure of molybdenum disulphide atomic layers. *Nat. Mater.* **2013**, *12*, 754–759.

[31] Ahn, C.; Lee, J.; Kim, H. U.; Bark, H.; Jeon, M.; Ryu, G. H.; Lee, Z.; Yeom, G. Y.; Kim, K.; Jung, J. et al. Low-temperature synthesis

of large-scale molybdenum disulfide thin films directly on a plastic substrate using plasma-enhanced chemical vapor deposition. *Adv. Mater.* **2015**, *27*, 5223–5229.

[32] Shaw, J. C.; Zhou, H.; Chen, Y.; Weiss, N. O.; Liu, Y.; Huang, Y.; Duan, X. Chemical vapor deposition growth of monolayer $MoSe_2$ nanosheets. *Nano Res.* **2014**, *7*, 511–517.

[33] Gao, Y.; Liu, Z. B.; Sun, D. M.; Huang, L.; Ma, L. P.; Yin, L. C.; Ma, T.; Zhang, Z. Y.; Ma, X. L.; Peng, L. M. et al. Large-area synthesis of high-quality and uniform monolayer WS_2 on reusable Au foils. *Nat. Commun.* **2015**, *6*, 8569.

[34] Tan, C. L.; Zhang, H. Wet-chemical synthesis and applications of non-layer structured two-dimensional nanomaterials. *Nat. Commun.* **2015**, *6*, 7873.

[35] Mamaghani, A. H.; Haghighat, F.; Lee, C. S. Hydrothermal/solvothermal synthesis and treatment of TiO_2 for photocatalytic degradation of air pollutants: Preparation, characterization, properties, and performance. *Chemosphere* **2019**, *219*, 804–825.

[36] Yoo, D.; Kim, M.; Jeong, S.; Han, J.; Cheon, J. Chemical synthetic strategy for single-layer transition-metal chalcogenides. *J. Am. Chem. Soc.* **2014**, *136*, 14670–14673.

[37] Xie, J. F.; Zhang, J. J.; Li, S.; Grote, F.; Zhang, X. D.; Zhang, H.; Wang, R. X.; Lei, Y.; Pan, B. C.; Xie, Y. Controllable disorder engineering in oxygen-incorporated MoS_2 ultrathin nanosheets for efficient hydrogen evolution. *J. Am. Chem. Soc.* **2013**, *135*, 17881–17888.

[38] Son, J. S.; Yu, J. H.; Kwon, S. G.; Lee, J.; Joo, J.; Hyeon, T. Colloidal synthesis of ultrathin two-dimensional semiconductor nanocrystals. *Adv. Mater.* **2011**, *23*, 3214–3219.

[39] Mak, K. F.; Shan, J. Photonics and optoelectronics of 2D semiconductor transition metal dichalcogenides. *Nat. Photonics* **2016**, *10*, 216–226.

[40] Eda, G.; Maier, S. A. Two-dimensional crystals: Managing light for optoelectronics. *ACS Nano* **2013**, *7*, 5660–5665.

[41] Dai, Z. G.; Hu, G. W.; Ou, Q. D.; Zhang, L.; Xia, F. N.; Garcia-Vidal, F. J.; Qiu, C. W.; Bao, Q. L. Artificial metaphotonics born naturally in two dimensions. *Chem. Rev.* **2020**, *120*, 6197–6246.

[42] Huang, T. Y.; Zhao, X.; Zeng, S. W.; Crunteanu, A.; Shum, P. P.; Yu, N. F. Planar nonlinear metasurface optics and their applications. *Rep. Prog. Phys.* **2020**, *83*, 126101.

[43] So, S.; Badloe, T.; Noh, J.; Bravo-Abad, J.; Rho, J. Deep learning enabled inverse design in nanophotonics. *Nanophotonics* **2020**, *9*, 1041–1057.

[44] Zhang, Y. C.; Jiang, Q. Q.; Lang, P.; Yuan, N. N.; Tang, J. G. Fabrication and applications of 2D black phosphorus in catalyst, sensing and electrochemical energy storage. *J. Alloys Compd.* **2021**, *850*, 156580.

[45] Niu, P.; Zhang, L. L.; Liu, G.; Cheng, H. M. Graphene-like carbon nitride nanosheets for improved photocatalytic activities. *Adv. Funct. Mater.* **2012**, *22*, 4763–4770.

[46] Li, H. N.; Li, Y.; Aljarb, A.; Shi, Y. M.; Li, L. J. Epitaxial growth of two-dimensional layered transition-metal dichalcogenides: Growth mechanism, controllability, and scalability. *Chem. Rev.* **2018**, *118*, 6134–6150.

[47] Zhou, J. D.; Lin, J. H.; Huang, X. W.; Zhou, Y.; Chen, Y.; Xia, J.; Wang, H.; Xie, Y.; Yu, H. M.; Lei, J. C. et al. A library of atomically thin metal chalcogenides. *Nature* **2018**, *556*, 355–359.

[48] Fiori, G.; Bonaccorso, F.; Iannaccone, G.; Palacios, T.; Neumaier, D.; Seabaugh, A.; Banerjee, S. K.; Colombo, L. Electronics based on two-dimensional materials. *Nat. Nanotechnol.* **2014**, *9*, 768–779.

[49] Koppens, F. H. L.; Mueller, T.; Avouris, P.; Ferrari, A. C.; Vitiello, M. S.; Polini, M. Photodetectors based on graphene, other two-dimensional materials and hybrid systems. *Nat. Nanotechnol.* **2014**, *9*, 780–793.

[50] Wang, Y. L.; Li, L. F.; Yao, W.; Song, S. R.; Sun, J. T.; Pan, J. B.; Ren, X.; Li, C.; Okunishi, E.; Wang, Y. Q. et al. Monolayer $PtSe_2$, a new semiconducting transition-metal-dichalcogenide, epitaxially grown by direct selenization of Pt. *Nano Lett.* **2015**, *15*, 4013–4018.

[51] Ciarrocchi, A.; Avsar, A.; Ovchinnikov, D.; Kis, A. Thickness-modulated metal-to-semiconductor transformation in a transition metal dichalcogenide. *Nat. Commun.* **2018**, *9*, 919.

[52] Wang, Z. G.; Li, Q.; Besenbacher, F.; Dong, M. D. Facile synthesis of single crystal $PtSe_2$ nanosheets for nanoscale electronics. *Adv. Mater.* **2016**, *28*, 10224–10229.

[53] Miró, P.; Ghorbani-Asl, M.; Heine, T. Two dimensional materials beyond MoS_2: Noble-transition-metal dichalcogenides. *Angew. Chem., Int. Ed.* **2014**, *53*, 3015–2018.

[54] Oyedele, A. D.; Yang, S. Z.; Liang, L. B.; Puretzky, A. A.; Wang, K.; Zheng, J. J.; Yu, P.; Pudasaini, P. R.; Ghosh, A. W.; Liu, Z. et al. $PdSe_2$: Pentagonal two-dimensional layers with high air stability for electronics. *J. Am. Chem. Soc.* **2017**, *139*, 14090–14097.

[55] Chow, W. L.; Yu, P.; Liu, F. C.; Hong, J. H.; Wang, X. L.; Zeng, Q. S.; Hsu, C. H.; Zhu, C.; Zhou, J. D.; Wang, X. W. et al. High mobility 2D palladium diselenide field-effect transistors with tunable ambipolar characteristics. *Adv. Mater.* **2017**, *29*, 1602969.

[56] Yu, X. C.; Yu, P.; Wu, D.; Singh, B.; Zeng, Q. S.; Lin, H.; Zhou, W.; Lin, J. H.; Suenaga, K.; Liu, Z. et al. Atomically thin noble metal dichalcogenide: A broadband mid-infrared semiconductor. *Nat. Commun.* **2018**, *9*, 1545.

[57] Wu, D.; Guo, J. W.; Du, J.; Xia, C. X.; Zeng, L. H.; Tian, Y. Z.; Shi, Z. F.; Tian, Y. T.; Li, X. J.; Tsang, Y. H. et al. Highly polarization-sensitive, broadband, self-powered photodetector based on Graphene/$PdSe_2$/Germanium heterojunction. *ACS Nano* **2019**, *13*, 9907–9917.

[58] Long, M. S.; Wang, Y.; Wang, P.; Zhou, X. H.; Xia, H.; Luo, C.; Huang, S. Y.; Zhang, G. W.; Yan, H. G.; Fan, Z. Y. et al. Palladium diselenide long-wavelength infrared photodetector with high sensitivity and stability. *ACS Nano* **2019**, *13*, 2511–2519.

[59] Yao, W.; Wang, E. Y.; Huang, H. Q.; Deng, K.; Yan, M. Z.; Zhang, K. N.; Miyamoto, K.; Okuda, T.; Li, L. F.; Wang, Y. L. et al. Direct observation of spin-layer locking by local Rashba effect in monolayer semiconducting $PtSe_2$ film. *Nat. Commun.* **2017**, *8*, 14216.

[60] Avsar, A.; Ciarrocchi, A.; Pizzochero, M.; Unuchek, D.; Yazyev, O. V.; Kis, A. Defect induced, layer-modulated magnetism in ultrathin metallic $PtSe_2$. *Nat. Nanotechnol.* **2019**, *14*, 674–678.

[61] Li, L.; Wang, W. K.; Chai, Y.; Li, H. Q.; Tian, M. L.; Zhai, T. Y. Few-layered PtS_2 phototransistor on h-BN with high gain. *Adv. Funct. Mater.* **2017**, *27*, 1701011.

[62] Zhao, Y. D.; Qiao, J. S.; Yu, Z. H.; Yu, P.; Xu, K.; Lau, S. P.; Zhou, W.; Liu, Z.; Wang, X. R.; Ji, W. et al. High-electron-mobility and air-stable 2D layered $PtSe_2$ FETs. *Adv. Mater.* **2017**, *29*, 1604230.

[63] Jiang, W.; Wang, X. D.; Chen, Y.; Wu, G. J.; Ba, K.; Xuan, N. N.; Sun, Y. Y.; Gong, P.; Bao, J. X.; Shen, H. et al. Large-area high quality $PtSe_2$ thin film with versatile polarity. *InfoMat* **2019**, *1*, 260–267.

[64] Yim, C.; Lee, K.; McEvoy, N.; O'Brien, M.; Riazimehr, S.; Berner, N. C.; Cullen, C. P.; Kotakoski, J.; Meyer, J. C.; Lemme, M. C. et al. High-performance hybrid electronic devices from layered $PtSe_2$ films grown at low temperature. *ACS Nano* **2016**, *10*, 9550–9558.

[65] Bao, Q. L.; Zhang, H.; Wang, Y.; Ni, Z. H.; Yan, Y. L.; Shen, Z. X.; Loh, K. P.; Tang, D. Y. Atomic-layer graphene as a saturable absorber for ultrafast pulsed lasers. *Adv. Funct. Mater.* **2009**, *19*, 3077–3083.

[66] Zeng, L. H.; Lin, S. H.; Li, Z. J.; Zhang, Z. X.; Zhang, T. F.; Xie, C.; Mak, C. H.; Chai, Y.; Lau, S. P.; Luo, L. B. et al. Fast, self-driven, air-stable, and broadband photodetector based on vertically aligned $PtSe_2$/GaAs heterojunction. *Adv. Funct. Mater.* **2018**, *28*, 1705970.

[67] Zeng, L. H.; Wu, D.; Lin, S. H.; Xie, C.; Yuan, H. Y.; Lu, W.; Lau, S. P.; Chai, Y.; Luo, L. B.; Li, Z. J. et al. Controlled synthesis of 2D palladium diselenide for sensitive photodetector applications. *Adv. Funct. Mater.* **2019**, *29*, 1806878.

[68] Chia, X.; Adriano, A.; Lazar, P.; Sofer, Z.; Luxa, J.; Pumera, M. Layered platinum dichalcogenides (PtS_2, $PtSe_2$, and $PtTe_2$) electrocatalysis: Monotonic dependence on the chalcogen size. *Adv. Funct. Mater.* **2016**, *26*, 4306–4318.

[69] Wang, Y. W.; Deng, Z. L.; Hu, D. J.; Yuan, J.; Ou, Q. D.; Qin, F.;

Zhang, Y. N.; Ouyang, X.; Li, Y.; Peng, B. et al. Atomically thin noble metal dichalcogenides for phase-regulated meta-optics. *Nano Lett.* **2020**, *20*, 7811–7818.

[70] Li, P. Y.; Zhang, J. T.; Zhu, C.; Shen, W. F.; Hu, C. G.; Fu, W.; Yan, L.; Zhou, L. J.; Zheng, L; Lei, H. X. et al. Penta-PdPSe: a new 2D pentagonal material with highly in-plane optical, electronic, and optoelectronic anisotropy. *Adv. Mater.* **2021**, *33*, 2102541.

[71] Ge, J.; Luo, T. C.; Lin, Z. Z.; Shi, J. P.; Liu, Y. Z.; Wang, P. Y.; Zhang, Y. F.; Duan, W. H.; Wang, J. Magnetic moments induced by atomic vacancies in transition metal dichalcogenide flakes. *Adv. Mater.* **2021**, *33*, 2005465.

[72] Wagner, S.; Yim, C.; McEvoy, N.; Kataria, S.; Yokaribas, V.; Kuc, A.; Pindl, S.; Fritzen, C. P.; Heine, T.; Duesberg, G. S. et al. Highly sensitive electromechanical piezoresistive pressure sensors based on large-area layered $PtSe_2$ films. *Nano Lett.* **2018**, *18*, 3738–3745.

[73] Yuan, J.; Mu, H. R.; Li, L.; Chen, Y.; Yu, W. Z.; Zhang, K.; Sun, B. Q.; Lin, S. H.; Li, S. J.; Bao, Q. L. Few-layer platinum diselenide as a new saturable absorber for ultrafast fiber lasers. *ACS Appl. Mater. Interfaces* **2018**, *10*, 21534–21540.

[74] Yang, H.; Kim, S. W.; Chhowalla, M.; Lee, Y. H. Structural and quantum-state phase transitions in van der Waals layered materials. *Nat. Phys.* **2017**, *13*, 931–937.

[75] Liu, C.; Lian, C. S.; Liao, M. H.; Wang, Y.; Zhong, Y.; Ding, C.; Li, W.; Song, C. L.; He, K.; Ma, X. C. et al. Two-dimensional superconductivity and topological states in $PdTe_2$ thin films. *Phys. Rev. Mater.* **2018**, *2*, 094001.

[76] Zhang, K. N.; Yan, M. Z.; Zhang, H. X.; Huang, H. Q.; Arita, M.; Sun, Z.; Duan, W. H.; Wu, Y.; Zhou, S. Y. Experimental evidence for type-II Dirac semimetal in $PtSe_2$. *Phys. Rev. B* **2017**, *96*, 125102.

[77] Cheng, P. K.; Tang, C. Y.; Wang, X. Y.; Ma, S. N.; Long, H.; Tsang, Y. H. Passively Q-switched Ytterbium-doped fiber laser based on broadband multilayer platinum ditelluride ($PtTe_2$) saturable absorber. *Sci. Rep.* **2019**, *9*, 10106.

[78] Yu, J.; Kuang, X. F.; Gao, Y. J.; Wang, Y. P.; Chen, K. Q.; Ding, Z. K.; Liu, J.; Cong, C. X.; He, J.; Liu, Z. W. et al. Direct observation of the linear dichroism transition in two-dimensional palladium diselenide. *Nano Lett.* **2020**, *20*, 1172–1182.

[79] Liang, Q.; Wang, Q. X.; Zhang, Q.; Wei, J. X.; Lim, S. X.; Zhu, R.; Hu, J. X.; Wei, W.; Lee, C.; Sow, C. et al. High-performance, room temperature, ultra-broadband photodetectors based on air-stable $PdSe_2$. *Adv. Mater.* **2019**, *31*, 1807609.

[80] Cheng, P. K.; Tang, C. Y.; Wang, X. Y.; Zeng, L. H.; Tsang, Y. H. Passively *Q*-switched and femtosecond mode-locked erbium-doped fiber laser based on a 2D palladium disulfide (PdS_2) saturable absorber. *Photon. Res.* **2020**, *8*, 511–518.

[81] Ma, Y. F.; Zhang, S. C.; Ding, S. J.; Liu, X. X.; Yu, X.; Peng, F.; Zhang, Q. L. Passively Q-switched Nd: $GdLaNbO_4$ laser based on 2D $PdSe_2$ nanosheet. *Opt. Laser Technol.* **2020**, *124*, 105959.

[82] Splendiani, A.; Sun, L.; Zhang, Y. B.; Li, T. S.; Kim, J.; Chim, C. Y.; Galli, G.; Wang, F. Emerging photoluminescence in monolayer MoS_2. *Nano Lett.* **2010**, *10*, 1271–1275.

[83] Zhao, Y. D.; Qiao, J. S.; Yu, P.; Hu, Z. X.; Lin, Z. Y.; Lau, S. P.; Liu, Z.; Ji, W.; Chai, Y. Extraordinarily strong interlayer interaction in 2D layered PtS_2. *Adv. Mater.* **2016**, *28*, 2399–2407.

[84] Villaos, R. A. B.; Crisostomo, C. P.; Huang, Z. Q.; Huang, S. M.; Padama, A. A. B.; Albao, M. A.; Lin, H.; Chuang, F. C. Thickness dependent electronic properties of Pt dichalcogenides. *npj 2D Mater. Appl.* **2019**, *3*, 2.

[85] Zhang, W. X.; Huang, Z. S.; Zhang, W. L.; Li, Y. R. Two-dimensional semiconductors with possible high room temperature mobility. *Nano Res.* **2014**, *7*, 1731–1737.

[86] Gu, Y. Y.; Cai, H.; Dong, J. C.; Yu, Y. L.; Hoffman, A. N.; Liu, C. Z.; Oyedele, A. D.; Lin, Y. C.; Ge, Z. Z.; Puretzky, A. A. et al. Two-dimensional palladium diselenide with strong in-plane optical anisotropy and high mobility grown by chemical vapor deposition. *Adv. Mater.* **2020**, *32*, 1906238.

[87] Sun, J. F.; Shi, H. L.; Siegrist, T.; Singh, D. J. Electronic, transport, and optical properties of bulk and mono-layer $PdSe_2$. *Appl. Phys. Lett.* **2015**, *107*, 153902.

[88] Wang, X. Y.; Qarony, W.; Cheng, P. K.; Ismail, M.; Tsang, Y. H. Photoluminescence of PdS_2 and $PdSe_2$ quantum dots. *RSC Adv.* **2019**, *9*, 38077–38084.

[89] Huang, B.; Clark, G.; Navarro-Moratalla, E.; Klein, D. R.; Cheng, R.; Seyler, K. L.; Zhong, D.; Schmidgall, E.; McGuire, M. A.; Cobden, D. H. et al. Layer-dependent ferromagnetism in a van der Waals crystal down to the monolayer limit. *Nature* **2017**, *546*, 270–273.

[90] Deng, Y. J.; Yu, Y. J.; Song, Y. C.; Zhang, J. Z.; Wang, N. Z.; Sun, Z. Y.; Yi, Y. F.; Wu, Y. Z.; Wu, S. W.; Zhu, J. Y. et al. Gate-tunable room-temperature ferromagnetism in two-dimensional Fe_3GeTe_2. *Nature* **2018**, *563*, 94–99.

[91] Huang, H. Q.; Zhou, S. Y.; Duan, W. H. Type-II Dirac fermions in the $PtSe_2$ class of transition metal dichalcogenides. *Phys. Rev. B* **2016**, *94*, 121117.

[92] Leng, H.; Ohmura, A.; Anh, L. N.; Ishikawa, F.; Naka, T.; Huang, Y. K.; de Visser, A. Superconductivity under pressure in the Dirac semimetal $PdTe_2$. *J. Phys.: Condens. Matter* **2020**, *32*, 025603.

[93] Li, K. L.; Wang, T. Y.; Wang, W. J.; Gao, X. G. Lattice vibration properties of MoS_2/$PtSe_2$ heterostructures. *J. Alloys Compd.* **2020**, *820*, 153192.

[94] Avsar, A.; Cheon, C. Y.; Pizzochero, M.; Tripathi, M.; Ciarrocchi, A.; Yazyev, O. V.; Kis, A. Probing magnetism in atomically thin semiconducting $PtSe_2$. *Nat. Commun.* **2020**, *11*, 4806.

[95] Cheng, C.; Sun, J. T.; Liu, M.; Chen, X. R.; Meng, S. Tunable electron–phonon coupling superconductivity in platinum diselenide. *Phys. Rev. Mater.* **2017**, *1*, 074804.

[96] Yuan, Y. H.; Duan, Y. X.; Wang, Z. W.; Sun, J. Filamentary superconductivity in wrinkled $PtSe_2$. *J. Phys. D:Appl. Phys.* **2021**, *54*, 215302.

[97] Zhu, R.; Gao, Z. B.; Liang, Q. J.; Hu, J. X.; Wang, J. S.; Qiu, C. W.; Wee, A. T. S. Observation of anisotropic magnetoresistance in layered nonmagnetic semiconducting $PdSe_2$. *ACS Appl. Mater. Interfaces* **2021**, *13*, 37527–37534.

[98] Xu, H.; Guo, C.; Zhang, J. Z.; Guo, W. L.; Kuo, C. N.; Lue, C. S.; Hu, W. D.; Wang, L.; Chen, G.; Politano, A. et al. $PtTe_2$-based type-II Dirac semimetal and its van der Waals heterostructure for sensitive room temperature terahertz photodetection. *Small* **2019**, *15*, 1903362.

[99] Anemone, G.; Garnica, M.; Zappia, M.; Aguilar, P. C.; Al Taleb, A.; Kuo, C. N.; Lue, C. S.; Politano, A.; Benedek, G.; de Parga, A. L. V. et al. Experimental determination of surface thermal expansion and electron–phonon coupling constant of 1T-$PtTe_2$. *2D Mater.* **2020**, *7*, 025007.

[100] Xu, H.; Zhang, H. M.; Liu, Y. W.; Zhang, S. M.; Sun, Y. Y.; Guo, Z. X.; Sheng, Y. C.; Wang, X. D.; Luo, C.; Wu, X. et al. Controlled doping of wafer-scale $PtSe_2$ films for device application. *Adv. Funct. Mater.* **2019**, *29*, 1805614.

[101] Yi, M.; Shen, Z. G. A review on mechanical exfoliation for the scalable production of graphene. *J. Mater. Chem. A* **2015**, *3*, 11700–11715.

[102] Sarkar, A. S.; Stratakis, E. Recent advances in 2D metal monochalcogenides. *Adv. Sci.* **2020**, *7*, 2001655.

[103] Huang, J. W.; Dong, N. N.; McEvoy, N.; Wang, L.; Coileáin, C. Ó.; Wang, H. Q.; Cullen, C. P.; Chen, C. D.; Zhang, S. F.; Zhang, L. et al. Surface-state assisted carrier recombination and optical nonlinearities in bulk to 2D nonlayered PtS. *ACS Nano* **2019**, *13*, 13390–13402.

[104] Wang, X. Y.; Cheng, P. K.; Tang, C. Y.; Long, H.; Yuan, H. Y.; Zeng, L. H.; Ma, S. N.; Qarony, W.; Tsang, Y. H. Laser Q-switching with PtS_2 microflakes saturable absorber. *Opt. Express* **2018**, *26*, 13055–13060.

[105] Hernandez, Y.; Nicolosi, V.; Lotya, M.; Blighe, F. M.; Sun, Z. Y.; De, S.; McGovern, I. T.; Holland, B.; Byrne, M.; Gun'ko, Y. K. et al. High-yield production of graphene by liquid-phase exfoliation of graphite. *Nat. Nanotechnol.* **2008**, *3*, 563–568.

[106] Li, H.; Wu, J.; Yin, Z. Y.; Zhang, H. Preparation and applications of mechanically exfoliated single-layer and multilayer MoS_2 and WSe_2 nanosheets. *Acc. Chem. Res.* **2014**, *47*, 1067–1075.

[107] Huo, C. X.; Yan, Z.; Song, X. F.; Zeng, H. B. 2D materials via

liquid exfoliation: A review on fabrication and applications. *Sci. Bull.* **2015**, *60*, 1994–2008.

[108] Xu, W. T.; Jiang, J. Y.; Ma, H. F.; Zhang, Z. W.; Li, J.; Zhao, B.; Wu, R. X.; Yang, X. D.; Zhang, H. M.; Li, B. L. et al. Vapor phase growth of two-dimensional $PdSe_2$ nanosheets for high-photoresponsivity near-infrared photodetectors. *Nano Res.* **2020**, *13*, 2091–2097.

[109] Azadmanjiri, J.; Berndt, C. C.; Wang, J.; Kapoor, A.; Srivastava, V. K. Nanolaminated composite materials: Structure, interface role and applications. *RSC Adv.* **2016**, *6*, 109361–109385.

[110] Tang, H. W.; Zhang, H. M.; Chen, X. Y.; Wang, Y.; Zhang, X. Z.; Cai, P. Y.; Bao, W. Z. Recent progress in devices and circuits based on wafer-scale transition metal dichalcogenides. *Sci. China Inf. Sci.* **2019**, *62*, 220401.

[111] Zhan, Y. J.; Liu, Z.; Najmaei, S.; Ajayan, P. M.; Lou, J. Large-area vapor-phase growth and characterization of MoS_2 atomic layers on a SiO_2 substrate. *Small* **2012**, *8*, 966–971.

[112] Wang, Z.; Wang, P.; Wang, F.; Ye, J. F.; He, T.; Wu, F.; Peng, M.; Wu, P. S.; Chen, Y. F.; Zhong, F. et al. A noble metal dichalcogenide for high-performance field-effect transistors and broadband photodetectors. *Adv. Funct. Mater.* **2020**, *30*, 1907945.

[113] Wu, J.; Zhao, Y. S.; Sun, M. L.; Zheng, M. R.; Zhang, G.; Liu, X. K.; Chi, D. Z. Enhanced photoresponse of highly air-stable palladium diselenide by thickness engineering. *Nanophotonics* **2020**, *9*, 2467–2474.

[114] Zhong, J. H.; Yu, J.; Cao, L. K.; Zeng, C.; Ding, J. N.; Cong, C. X.; Liu, Z. W.; Liu, Y. P. High-performance polarization-sensitive photodetector based on a few-layered $PdSe_2$ nanosheet. *Nano Res.* **2020**, *13*, 1780–1786.

[115] Long, H.; Tang, C. Y.; Cheng, P. K.; Wang, X. Y.; Qarony, W.; Tsang, Y. H. Ultrafast laser pulses generation by using 2D layered PtS_2 as a saturable absorber. *J. Lightwave Technol.* **2019**, *37*, 1174–1179.

[116] Hoffman, A. N.; Gu, Y. Y.; Liang, L. B.; Fowlkes, J. D.; Xiao, K.; Rack, P. D. Exploring the air stability of $PdSe_2$ via electrical transport measurements and defect calculations. *npj 2D Mater. Appl.* **2019**, *3*, 50.

[117] Jiang, S. L.; Xie, C. Y.; Gu, Y.; Zhang, Q. H.; Wu, X. X.; Sun, Y. L.; Li, W.; Shi, Y. P.; Zhao, L. Y.; Pan, S. Y. et al. Anisotropic growth and scanning tunneling microscopy identification of ultrathin even-layered $PdSe_2$ ribbons. *Small* **2019**, *15*, 1902789.

[118] Yuan, J.; Sun, T.; Hu, Z. X.; Yu, W. Z.; Ma, W. L.; Zhang, K.; Sun, B. Q.; Lau, S. P.; Bao, Q. L.; Lin, S. H. et al. Wafer-scale fabrication of two-dimensional $PtS_2/PtSe_2$ heterojunctions for efficient and broad band photodetection. *ACS Appl. Mater. Interfaces* **2018**, *10*, 40614–40622.

[119] Zhao, D. H.; Xie, S.; Wang, Y.; Zhu, H.; Chen, L.; Sun, Q. Q.; Zhang, D. W. Synthesis of large-scale few-layer PtS_2 films by chemical vapor deposition. *AIP Adv.* **2019**, *9*, 025225.

[120] Ansari, L.; Monaghan, S.; McEvoy, N.; Coileáin, C. Ó.; Cullen, C. P.; Lin, J.; Siris, R.; Stimpel-Lindner, T.; Burke, K. F.; Mirabelli, G. et al. Quantum confinement-induced semimetal-to-semiconductor evolution in large-area ultra-thin $PtSe_2$ films grown at 400 °C. *npj 2D Mater. Appl.* **2019**, *3*, 33.

[121] Yim, C.; Passi, V.; Lemme, M. C.; Duesberg, G. S.; Coileáin, C. Ó.; Pallecchi, E.; Fadil, D.; McEvoy, N. Electrical devices from top-down structured platinum diselenide films. *npj 2D Mater. Appl.* **2018**, *2*, 5.

[122] Wang, L.; Zhang, S. F.; McEvoy, N.; Sun, Y. Y.; Huang, J. W.; Xie, Y. F.; Dong, N. N.; Zhang, X. Y.; Kislyakov, I. M.; Nunzi, J. M. et al. Nonlinear optical signatures of the transition from semiconductor to semimetal in $PtSe_2$. *Laser Photon. Rev.* **2019**, *13*, 1900052.

[123] Zeng, L. H.; Lin, S. H.; Lou, Z. H.; Yuan, H. Y.; Long, H.; Li, Y. Y.; Lu, W.; Lau, S. P.; Wu, D.; Tsang, Y. H. Ultrafast and sensitive photodetector based on a $PtSe_2$/silicon nanowire array heterojunction with a multiband spectral response from 200 to 1550 nm. *NPG Asia Mater.* **2018**, *10*, 352–362.

[124] Wu, D.; Wang, Y. G.; Zeng, L. H.; Jia, C.; Wu, E. P.; Xu, T. T.; Shi, Z. F.; Tian, Y. T.; Li, X. J.; Tsang, Y. H. Design of 2D layered $PtSe_2$ heterojunction for the high-performance, room-temperature, broadband, infrared photodetector. *ACS Photonics* **2018**, *5*, 3820–3827.

[125] Zhang, Z. X.; Zeng, L. H.; Tong, X. W.; Gao, Y.; Xie, C.; Tsang, Y. H.; Luo, L. B.; Wu, Y. C. Ultrafast, Self-driven, and air-stable photodetectors based on multilayer $PtSe_2$/perovskite heterojunctions. *J. Phys. Chem. Lett.* **2018**, *9*, 1185–1194.

[126] Xie, C.; Zeng, L. H.; Zhang, Z. X.; Tsang, Y. H.; Luo, L. B.; Lee, J. H. High-performance broadband heterojunction photodetectors based on multilayered $PtSe_2$ directly grown on a Si substrate. *Nanoscale* **2018**, *10*, 15285–15293.

[127] Tao, L. L.; Huang, X. W.; He, J. S.; Lou, Y. J.; Zeng, L. H.; Li, Y. H.; Long, H.; Li, J. B.; Zhang, L.; Tsang, Y. H. Vertically standing $PtSe_2$ film: A saturable absorber for a passively mode-locked Nd: $LuVO_4$ laser. *Photon. Res.* **2018**, *6*, 750–755.

[128] Luo, L. B.; Wang, D.; Xie, C.; Hu, J. G.; Zhao, X. Y.; Liang, F. X. $PdSe_2$ multilayer on germanium nanocones array with light trapping effect for sensitive infrared photodetector and image sensing application. *Adv. Funct. Mater.* **2019**, *29*, 1900849.

[129] Zhang, K. N.; Wang, M.; Zhou, X.; Wang, Y.; Shen, S. C.; Deng, K.; Peng, H. N.; Li, J. H.; Lai, X. B.; Zhang, L. W. et al. Growth of large scale PtTe, $PtTe_2$ and $PtSe_2$ films on a wide range of substrates. *Nano Res.* **2020**, *14*, 1663–1667.

[130] Yan, M. Z.; Wang, E. Y.; Zhou, X.; Zhang, G. Q.; Zhang, H. Y.; Zhang, K. N.; Yao, W.; Lu, N. P.; Yang, S. Z.; Wu, S. L. et al. High quality atomically thin $PtSe_2$ films grown by molecular beam epitaxy. *2D Mater.* **2017**, *4*, 045015.

[131] Xiong, K. C.; Hilse, M.; Li, L.; Göritz, A.; Lisker, M.; Wietstruck, M.; Kaynak, M.; Engel-Herbert, R.; Madjar, A.; Hwang, J. C. M. Large-scale fabrication of submicrometer-gate-length MOSFETs with a trilayer $PtSe_2$ channel grown by molecular beam epitaxy. *IEEE Trans. Electron Devices* **2020**, *67*, 796–801.

[132] Li, E.; Zhang, R. Z.; Li, H.; Liu, C.; Li, G.; Wang, J. O.; Qian, T.; Ding, H.; Zhang, Y. Y.; Du, S. X. et al. High quality $PdTe_2$ thin films grown by molecular beam epitaxy. *Chin. Phys. B* **2018**, *27*, 086804.

[133] Li, E.; Wang, D. F.; Fan, P.; Zhang, R. Z.; Zhang, Y. Y.; Li, G.; Mao, J. H.; Wang, Y. L.; Lin, X.; Du, S. X. et al. Construction of bilayer $PdSe_2$ on epitaxial graphene. *Nano Res.* **2018**, *11*, 5858–5865.

[134] Nguyen, D. A.; Park, D. Y.; Lee, J.; Duong, N. T.; Park, C.; Nguyen, D. H.; Le, T. S.; Suh, D.; Yang, H.; Jeong, M. S. Patterning of type-II Dirac semimetal $PtTe_2$ for optimized interface of tellurene optoelectronic device. *Nano Energy* **2021**, *86*, 106049.

[135] Poh, S. M.; Zhao, X. X.; Tan, S. J. R.; Fu, D. Y.; Fei, W. W.; Chu, L. Q.; Jiadong, D.; Zhou, W.; Pennycook, S. J.; Neto, A. H. C. et al. Molecular beam epitaxy of highly crystalline $MoSe_2$ on hexagonal boron nitride. *ACS Nano* **2018**, *12*, 7562–7570.

[136] Gordon, R. A.; Yang, D.; Crozier, E. D.; Jiang, D. T.; Frindt, R. F. Structures of exfoliated single layers of WS_2, MoS_2, and $MoSe_2$ in aqueous suspension. *Phys. Rev. B* **2002**, *65*, 125407.

[137] Kirmayer, S.; Aharon, E.; Dovgolevsky, E.; Kalina, M.; Frey, G. L. Self-assembled lamellar MoS_2, SnS_2 and SiO_2 semiconducting polymer nanocomposites. *Philos. Trans. A Math. Phy. Eng. Sci.* **2007**, *365*, 1489–1508.

[138] Wang, Y. D.; Wang, Y. Y.; Chen, K. Q.; Qi, K.; Xue, T. Y.; Zhang, H.; He, J.; Xiao, S. Niobium carbide MXenes with broad-band nonlinear optical response and ultrafast carrier dynamics. *ACS Nano* **2020**, *14*, 10492–40502.

[139] Zhang, H.; Lu, S. B.; Zheng, J.; Du, J.; Wen, S. C.; Tang, D. Y.; Loh, K. P. Molybdenum disulfide (MoS_2) as a broadband saturable absorber for ultra-fast photonics. *Opt. Express* **2014**, *22*, 7249–7260.

[140] Mao, D.; Wang, Y. D.; Ma, C. J.; Han, L.; Jiang, B. Q.; Gan, X. T.; Hua, S. J.; Zhang, W. D.; Mei, T.; Zhao, J. L. WS_2 mode-locked ultrafast fiber laser. *Sci. Rep.* **2015**, *5*, 7965.

[141] Mu, H. R.; Lin, S. H.; Wang, Z. C.; Xiao, S.; Li, P. F.; Chen, Y.; Zhang, H.; Bao, H. F.; Lau, S. P.; Pan, C. X. et al. Black phosphorus-polymer composites for pulsed lasers. *Adv. Opt. Mater.* **2015**, *3*, 1447–1453.

[142] Luo, Z. Q.; Wu, D. D.; Xu, B.; Xu, H. Y.; Cai, Z. P.; Peng, J.; Weng, J.; Xu, S.; Zhu, C. H.; Wang, F. Q. et al. Two-dimensional material-based saturable absorbers: Towards compact visible-wavelength all-fiber pulsed lasers. *Nanoscale* **2016**, *8*, 1066–1072.

[143] Yu, J.; Kuang, X. F.; Li, J. Z.; Zhong, J. H.; Zeng, C.; Cao, L. K.; Liu, Z. W.; Zeng, Z. X. S.; Luo, Z. Y.; He, T. C. et al. Giant nonlinear optical activity in two-dimensional palladium diselenide. *Nat. Commun.* **2021**, *12*, 1083.

[144] Han, J.; Wang, Y. W.; He, J.; Lu, H.; Li, X. P.; Gu, M.; Zhang, Y. N. Fabry-Perot cavity enhanced three-photon luminescence of atomically thin platinum diselenide. *Nanoscale* **2021**, *13*, 9031–9038.

[145] Khan, K.; Tareen, A. K.; Aslam, M.; Wang, R. H.; Zhang, Y. P.; Mahmood, A.; Ouyang, Z. B.; Zhang, H.; Guo, Z. Y. Recent developments in emerging two-dimensional materials and their applications. *J. Mater. Chem. C* **2020**, *8*, 387–440.

[146] Syedmoradi, L.; Ahmadi, A.; Norton, M. L.; Omidfar, K. A review on nanomaterial-based field effect transistor technology for biomarker detection. *Microchim. Acta* **2019**, *186*, 739.

[147] Radisavljevic, B.; Radenovic, A.; Brivio, J.; Giacometti, V.; Kis, A. Single-layer MoS_2 transistors. *Nat. Nanotechnol.* **2011**, *6*, 147–150.

[148] Kaasbjerg, K.; Thygesen, K. S.; Jacobsen, K. W. Phonon-limited mobility in *n*-type single-layer MoS_2 from first principles. *Phys. Rev. B* **2012**, *85*, 115317.

[149] Xue, Y. Z.; Zhang, Y. P.; Liu, Y.; Liu, H. T.; Song, J. C.; Sophia, J.; Liu, J. Y.; Xu, Z. Q.; Xu, Q. Y.; Wang, Z. Y. et al. Scalable production of a few-layer MoS_2/WS_2 vertical heterojunction array and its application for photodetectors. *ACS Nano* **2016**, *10*, 573–580.

[150] Wood, J. D.; Wells, S. A.; Jariwala, D.; Chen, K. S.; Cho, E.; Sangwan, V. K.; Liu, X. L.; Lauhon, L. J.; Marks, T. J.; Hersam, M. C. Effective passivation of exfoliated black phosphorus transistors against ambient degradation. *Nano Lett.* **2014**, *14*, 6964–6970.

[151] Dean, C. R.; Young, A. F.; Meric, I.; Lee, C.; Wang, L.; Sorgenfrei, S.; Watanabe, K.; Taniguchi, T.; Kim, P.; Shepard, K. L. et al. Boron nitride substrates for high-quality graphene electronics. *Nat. Nanotechnol.* **2010**, *5*, 722–726.

[152] Cui, X.; Lee, G. H.; Kim, Y. D.; Arefe, G.; Huang, P. Y.; Lee, C. H.; Chenet, D. A.; Zhang, X.; Wang, L.; Ye, F. et al. Multi-terminal transport measurements of MoS_2 using a van der Waals heterostructure device platform. *Nat. Nanotechnol.* **2015**, *10*, 534–540.

[153] Li, L. K.; Yang, F. Y.; Ye, G. J.; Zhang, Z. C.; Zhu, Z. W.; Lou, W. K.; Zhou, X. Y.; Li, L.; Watanabe, K.; Taniguchi, T. et al. Quantum Hall effect in black phosphorus two-dimensional electron system. *Nat. Nanotechnol.* **2016**, *11*, 593–597.

[154] Liang, F. X.; Zhao, X. Y.; Jiang, J. J.; Hu, J. G.; Xie, W. Q.; Lv, J.; Zhang, Z. X.; Wu, D.; Luo, L. B. Light confinement effect induced highly sensitive, self-driven near-infrared photodetector and image sensor based on multilayer $PdSe_2$/pyramid Si heterojunction. *Small* **2019**, *15*, 1903831.

[155] Son, J. G.; Son, M.; Moon, K. J.; Lee, B. H.; Myoung, J. M.; Strano, M. S.; Ham, M. H.; Ross, C. A. Sub-10 nm graphene nanoribbon array field-effect transistors fabricated by block copolymer lithography. *Adv. Mater.* **2013**, *25*, 4723–4728.

[156] Amani, M.; Regan, E.; Bullock, J.; Ahn, G. H.; Javey, A. Mid-wave infrared photoconductors based on black phosphorus-arsenic alloys. *ACS Nano* **2017**, *11*, 11724–11731.

[157] Zeng, L. H.; Wu, D.; Jie, J. S.; Ren, X. Y.; Hu, X.; Lau, S. P.; Chai, Y.; Tsang, Y. H. Van der Waals epitaxial growth of mosaic-like 2D platinum ditelluride layers for room-temperature mid-infrared photodetection up to 10. 6 μm. *Adv. Mater.* **2020**, *32*, 2004412.

[158] Liu, Q. F.; Cook, B.; Gong, M. G.; Gong, Y. P.; Ewing, D.; Casper, M.; Stramel, A.; Wu, J. Printable transfer-free and wafer-size MoS_2/graphene van der Waals heterostructures for high-performance photodetection. *ACS Appl. Mater. Interfaces* **2017**, *9*, 12728–12733.

[159] Song, X. F.; Liu, X. H.; Yu, D. J.; Huo, C. X.; Ji, J. P.; Li, X. M.; Zhang, S. L.; Zou, Y. S.; Zhu, G. Y.; Wang, Y. J. et al. Boosting two-dimensional $MoS_2/CsPbBr_3$ photodetectors via enhanced light absorbance and interfacial carrier separation. *ACS Appl. Mater. Interfaces* **2018**, *10*, 2801–2809.

[160] Pi, L. J.; Li, L.; Liu, K. L.; Zhang, Q. F.; Li, H. Q.; Zhai, T. Y. Recent progress on 2D noble-transition-metal dichalcogenides. *Adv. Funct. Mater.* **2019**, *29*, 1904932.

[161] Li, Z. Q.; Li, R.; Pang, C.; Dong, N. N.; Wang, J.; Yu, H. H.; Chen, F. 8. 8 GHz Q-switched mode-locked waveguide lasers modulated by $PtSe_2$ saturable absorber. *Opt. Express* **2019**, *27*, 8727–8737.

[162] Huang, B.; Du, L.; Yi, Q.; Yang, L. L.; Li, J.; Miao, L. L.; Zhao, C. J.; Wen, S. C. Bulk-structured $PtSe_2$ for femtosecond fiber laser mode-locking. *Opt. Express* **2019**, *27*, 2604–2611.

[163] Yan, B. Z.; Zhang, B. T.; Nie, H. K.; Li, G. R.; Liu, J. T.; Shi, B. N.; Yang, K. J.; He, J. L. Bilayer platinum diselenide saturable absorber for 2. 0 μm passively Q-switched bulk lasers. *Opt. Express* **2018**, *26*, 31657–31663.

[164] Zhang, K.; Feng, M.; Ren, Y. Y.; Liu, F.; Chen, X. S.; Yang, J.; Yan, X. Q.; Song, F.; Tian, J. G. *Q*-switched and mode-locked Er-doped fiber laser using $PtSe_2$ as a saturable absorber. *Photon. Res.* **2018**, *6*, 893–899.

[165] Cui, N.; Zhang, F.; Zhao, Y. Q.; Yao, Y. P.; Wang, Q. G.; Dong, L. L.; Zhang, H. Y.; Liu, S. D.; Xu, J. L.; Zhang, H. The visible nonlinear optical properties and passively Q-switched laser application of a layered $PtSe_2$ material. *Nanoscale* **2020**, *12*, 1061–1066.

[166] Cheng, P. K.; Tang, C. Y.; Ahmed, S.; Qiao, J. P.; Zeng, L. H.; Tsang, Y. H. Utilization of group 10 2D TMDs-$PdSe_2$ as a nonlinear optical material for obtaining switchable laser pulse generation modes. *Nanotechnology* **2021**, *32*, 055201.

[167] Xu, N. N.; Wang, H. F.; Zhang, H. N.; Guo, L. G.; Shang, X. X.; Jiang, S. Z.; Li, D. W. Palladium diselenide as a direct absorption saturable absorber for ultrafast mode-locked operations: From all anomalous dispersion to all normal dispersion. *Nanophotonics* **2020**, *9*, 4295–4306.

[168] Zhang, H. N.; Ma, P. F.; Zhu, M. X.; Zhang, W. F.; Wang, G. M.; Fu, S. G. Palladium selenide as a broadband saturable absorber for ultra-fast photonics. *Nanophotonics* **2020**, *9*, 2557–2567.

[169] Su, T. Y.; Medina, H.; Chen, Y. Z.; Wang, S. W.; Lee, S. S.; Shih, Y. C.; Chen, C. W.; Kuo, H. C.; Chuang, F. C.; Chueh, Y. L. Phase-engineered $PtSe_2$ -layered films by a plasma-assisted selenization process toward all $PtSe_2$ -based field effect transistor to highly sensitive, flexible, and wide-spectrum photoresponse photodetectors. *Small* **2018**, *14*, 1800032.

[170] Yang, Y. J.; Jang, S. K.; Choi, H.; Xu, J.; Lee, S. Homogeneous platinum diselenide metal/semiconductor coplanar structure fabricated by selective thickness control. *Nanoscale* **2019**, *11*, 21068–21073.

[171] Lu, L. S.; Chen, G. H.; Cheng, H. Y.; Chuu, C. P.; Lu, K. C.; Chen, C. H.; Lu, M. Y.; Chuang, T. H.; Wei, D. H.; Chueh, W. C. et al. Layer-dependent and in-plane anisotropic properties of low-temperature synthesized few-layer $PdSe_2$ single crystals. *ACS Nano* **2020**, *14*, 4963–4972.

[172] Walmsley, T. S.; Andrews, K.; Wang, T. J.; Haglund, A.; Rijal, U.; Bowman, A.; Mandrus, D.; Zhou, Z. X.; Xu, Y. Q. Near-infrared optical transitions in $PdSe_2$ phototransistors. *Nanoscale* **2019**, *11*, 14410–14416.

[173] Afzal, A. M.; Iqbal, M. Z.; Dastgeer, G.; ul Ahmad, A.; Park, B. Highly sensitive, ultrafast, and broadband photo-detecting field-effect transistor with transition-metal dichalcogenide van der Waals heterostructures of $MoTe_2$ and $PdSe_2$. *Adv. Sci.* **2021**, *8*, 2003713.

[174] Tan, C. Y.; Yin, S. Q.; Chen, J. W.; Lu, Y.; Wei, W. S.; Du, H. F.; Liu, K. K.; Wang, F. K.; Zhai, T. Y.; Li, L. Broken-gap PtS_2/WSe_2 van der Waals heterojunction with ultrahigh reverse rectification and fast photoresponse. *ACS Nano* **2021**, *15*, 8328–8337.

[175] Zhuo, R. R.; Zeng, L. H.; Yuan, H. Y.; Wu, D.; Wang, Y. G.; Shi, Z. F.; Xu, T. T.; Tian, Y. T.; Li, X. J.; Tsang, Y. H. *In-situ* fabrication of $PtSe_2$/GaN heterojunction for self-powered deep ultraviolet photodetector with ultrahigh current on/off ratio and detectivity. *Nano Res.* **2019**, *12*, 183–189.

[176] Wang, Y.; Yu, Z. J.; Tong, Y. Y.; Sun, B. L.; Zhang, Z. Y.; Xu, J. B.; Sun, X. K.; Tsang, H. K. High-speed infrared two-dimensional platinum diselenide photodetectors. *Appl. Phys. Lett.* **2020**, *116*, 211101.

[177] Wang, Z.; Xia, H.; Wang, P.; Zhou, X. H.; Liu, C. S.; Zhang, Q. H.; Wang, F.; Huang, M. L.; Chen, S. Y.; Wu, P. S. et al. Controllable doping in 2D layered materials. *Adv. Mater.* **2021**, 2104942.

[178] Lin, Z. P.; Xiao, B. B.; Wang, Z. P.; Tao, W. Y.; Shen, S. J.; Huang, L. G.; Zhang, J. T.; Meng, F. Q.; Zhang, Q. H.; Gu, L. et al. Planar-coordination $PdSe_2$ nanosheets as highly active electrocatalyst for hydrogen evolution reaction. *Adv. Funct. Mater.* **2021**, *31*, 2102321.

[179] Wei, K. K.; Li, D. L.; Lin, Z. T.; Cheng, Z.; Yao, Y. H.; Guo, J.; Wang, Y. Z.; Zhang, Y. P.; Dong, J. J.; Zhang, H. et al. All-optical $PtSe_2$ silicon photonic modulator with ultra-high stability. *Photon. Res.* **2020**, *8*, 1189–1196.

[180] Chung, C. C.; Yeh, H.; Wu, P. H.; Lin, C. C.; Li, C. S.; Yeh, T. T.; Chou, Y.; Wei, C. Y.; Wen, C. Y.; Chou, Y. C. et al. Atomic-layer controlled interfacial band engineering at two-dimensional layered $PtSe_2$/Si heterojunctions for efficient photoelectrochemical hydrogen production. *ACS Nano* **2021**, *15*, 4627–4635.

[181] Kireev, D.; Okogbue, E.; Jayanth, R. T.; Ko, T. J.; Jung, Y.; Akinwande, D. Multipurpose and reusable ultrathin electronic tattoos based on $PtSe_2$ and $PtTe_2$. *ACS Nano* **2021**, *15*, 2800–2811.

[182] Ping, X. F.; Liang, D.; Wu, Y. Y.; Yan, X. X.; Zhou, S. X.; Hu, D. K.; Pan, X. Q.; Lu, P. F.; Jiao, L. Y. Activating a two-dimensional $PtSe_2$ basal plane for the hydrogen evolution reaction through the simultaneous generation of atomic vacancies and Pt clusters. *Nano Lett.* **2021**, *21*, 3857–3863.